Contributions to Mineralogy and Petrology (2024) 179:31
https://doi.org/10.1007/s00410-024-02108-1

ORIGINAL PAPER

Crystallisation of trapped carbonate–silicate melts terminating at the carbonated solidus ledge: a record of carbon immobilisation mechanism in the lithospheric mantle

Jakub Haifler[1] · **Jana Kotková**[2] · **Renata Čopjaková**[1]

Received: 14 August 2023 / Accepted: 1 February 2024 / Published online: 19 March 2024

Abstract

Orogenic peridotites in the crystalline basement of the northwestern Bohemian Massif contain multiphase solid inclusions (MSI), which are interpreted to be crystallisation products of trapped former carbonate–silicate melts metasomatizing their host rocks. We applied conventional thermobarometry and forward thermodynamic modelling to constrain the P–T evolution ranging from the peak metamorphic conditions of the investigated harzburgite and lherzolite, through entrapment of the melts in the outer parts of garnets, to the (re)-equilibration of the MSI assemblages. The peak conditions of c. 1100 °C/4.5–5.5 GPa are recorded by garnet cores and large pyroxene porphyroclasts. The melt entrapment, during which garnet outer parts grew, was associated with influx of the metasomatizing liquids and probably took place during the early stage of the exhumation. Thermodynamic model of amphibole-free MSI assemblage comprising *kinoshitalite/Ba-rich phlogopite* (approximated by *phlogopite* in the model), *dolomite, magnesite, clinopyroxene, orthopyroxene, garnet* and *chromite* provided robust estimate of P and T of its (re)-equilibration, c. 900–1000 °C, 1.8–2.2 GPa. Furthermore, the lack of olivine reflects co-existence of COH fluid with high $X(CO_2) = CO_2/(CO_2 + H_2O) \geq 0.6$. Models employing identical P–T–$X(CO_2)$ parameters successfully reproduced the other two amphibole-bearing assemblages observed. The modelled stability fields show perfect alignment with a characteristic isobaric segment of the solidus curve of carbonated peridotite. This co-incidence implies that the (re)-equilibration corresponds to the termination of the melt crystallisation once the near-isothermal exhumation path intersected the solidus. Decreased solubility of silicates at the carbonated peridotite "solidus ledge", inferred from the published experimental data, as well as concentric textures of some MSI indicates sequential crystallisation from the early silicates to late dolomite. The carbonated "solidus ledge" is a relatively narrow boundary in the lithospheric mantle capable of an abrupt immobilisation of fluxing or transported carbonated melts. The investigated rocks are estimated to store approximately 0.02 kg C/m^3 (or 6 ppm C) occurring as carbonates in the MSI.

Keywords Orogenic garnet peridotites · Bohemian Massif · Multiphase solid inclusions · Carbonated peridotite solidus · Pseudosection · Mantle melt

Introduction

Orogenic peridotites exposed in UHP (ultrahigh-pressure) terranes contain important records of processes in convergent settings, occurring within mantle wedge or at the interface between the wedge and the subducting slab. These tectonic settings play a crucial role in global cycles of volatiles and incompatible elements, including carbon (e.g. Spandler and Pirard 2013; Gibson and McKenzie 2023). Depending on the thermal structure of the subduction zone and the extent of the slab hydration, significant amounts of subducting solid forms of carbon may undergo transformation to a liquid phase via decarbonization, dissolution in hydrous

Communicated by Dante Canil.

✉ Jakub Haifler
haifler.j@mail.muni.cz

[1] Department of Geological Sciences, Masaryk University, Kotlářská 2, 611 37 Brno, Czech Republic

[2] Czech Geological Survey, Klárov 3, 118 21 Prague 1, Czech Republic

fluids or partial melting (e.g. Kerrick and Connolly 2001; Gorman et al. 2006; Johnston et al. 2011; Scambelluri et al. 2016; Martin and Hermann 2018). Influx of these highly mobile forms of carbon (and other elements) into overlying ultramafic mantle wedge rocks may cause extensive metasomatism due to significant gradients in chemical potential, redox and temperature (e.g. Cannaò and Malaspina 2018). Furthermore, elevated amounts of H_2O and CO_2 in the metasomatizing liquids (hereafter called COH fluids) and their relatively oxidising character, contrasting with the unaltered ambient mantle (Foley 2011; Cannaò and Malaspina 2018), decrease the solidus temperatures of the ultramafic lithologies significantly, below 1000 °C (Wallace and Green 1988; Foley et al. 2009; Foley 2011; Tumiati et al. 2013). Given that the thermal regime of the mantle wedge is characterised by temperatures exceeding these values (Currie and Hyndman 2006; Syracuse et al. 2010), redox/carbonated/hydrated partial melting of supra-subduction mantle peridotites may take place and produce carbonated and hydrated magmas (Foley et al. 2009; Foley 2011; Hammouda and Keshav 2015; Hammouda et al. 2021; Pintér et al. 2021).

However, field occurrences of appropriate samples recording these processes are relatively rare, as rising carbonated magmas tend to outgas before reaching the surface (Wallace 2005). Thus, the mechanisms of the melt generation, the characteristics of these melts, their evolution including the recognised link to the arc magmas, and their role in the global carbon cycle (e.g. Arculus and Powell 1986; Spandler and Pirard 2013; Codillo et al. 2018; Lara and Dasgupta 2022) remain poorly understood.

Multiphase solid inclusions (MSI) trapped in garnet or spinel in ultramafic mantle rocks represent tiny but unique witnesses of mantle metasomatism and melting, and liquid evolution through interaction with the surrounding mantle (e.g. Carswell and van Roermund 2005; Malaspina et al. 2006; Naemura et al. 2018; Ackerman et al. 2020; Kotková et al. 2021a). In this study, we investigated MSI in garnet in several garnet peridotite samples from borehole T-7 in northwestern Bohemian Massif. The MSI in selected samples contain rare low-variance carbonate–silicate mineral assemblages favourable for thermobarometry and thermodynamic modelling. The host rocks occur as tectonic fragments of orogenic peridotites juxtaposed with diamond- and coesite-bearing continental crustal rocks. Together, they represent UHP and UHT terrane and reflect formation in a hot subduction zone (Medaris et al. 2015; Kotková et al. 2021b).

Recently, Kotková et al. (2021a) demonstrated that the MSI represent residual carbonate- and silicate-bearing liquids derived from garnet pyroxenite intruding garnet peridotite. The liquids gradually evolved during percolative infiltration into the adjacent garnet peridotites, in which they were trapped in garnet. Here, we extend their study aiming to constrain the unexplored post-entrapment evolution of these liquids and to address their role in the transport/storage of carbon in the lithospheric mantle. We show that the P–T conditions, at which the liquids were generated and trapped, exceeded experimentally determined solid carbonated and hydrated ultramafic rocks (e.g. Wallace and Green 1988; Foley et al. 2009; Pintér et al. 2021). In several aspects, we interpret the trapped liquids as chemically more complex natural analogues of these low-degree experimental carbonate–silicate melts. They share common features, including their carbonate–silicate nature, similar protoliths/precursors (peridotite + COH fluids), and presumably, comparable P–T conditions at which are stable. However, the mechanisms controlling the genesis and evolution of our investigated former melts were much more complex and mostly different. Whilst the experiments largely simulate production and evolution of the incipient carbonated melts during the partial melting of peridotites at rising temperatures, the studied MSI and their hosts were shown to reveal processes of the evolution of the carbonate–silicate melts, controlled by exhumation of the host rocks, terminating in complete melt crystallisation.

We applied conventional thermobarometry and thermodynamic modelling to evaluate equilibrium amongst minerals present in the MSI and to constrain the P–T conditions of their (re-)equilibration. Furthermore, co-existence of COH fluid with the solid phases and its composition was addressed. We also revaluated the peak P–T conditions of the host rocks using preserved larger pyroxene grains, not considered in the previous estimates (Medaris et al. 2015), and derived a comprehensive P–T exhumation path, not previously defined for the mantle rocks. We discussed evolution of the trapped melts along the exhumation path, and the relationship between the stability fields of the equilibrium assemblages in the MSI and the experimentally determined solidi of carbonated melts.

We point out that the observed inclusions of trapped former melts serve as petrological evidence of a mechanism that immobilises liquid carbon in the lithospheric mantle.

Garnet peridotites from the T-7 borehole and multiphase solid inclusions in their garnets

The multiphase solid inclusions (MSI) were discovered in garnet in garnet peridotites and an associated garnet pyroxenite vein in T-7 borehole in the Saxothuringian Zone in the northwestern Bohemian Massif. Čopjaková and Kotková (2018) and Kotková et al. (2021a) provided a detailed description of the mineralogy and bulk chemical composition of the MSI.

The host garnet peridotites represent tectonic fragments of the lithospheric mantle incorporated into a complex of

(ultra)high-pressure continental crustal rocks during their deep subduction to mantle depths (e.g. Kotková et al. 2011; Medaris et al. 2015). The sampled garnet peridotite body is c. 114 m thick, but occurs at depths ranging from 209 to 437 m due to its inclination. It comprises alternating decameter—to several metres thick layers of lherzolite predominating over harzburgite and several layers of eclogite. A scarce garnet pyroxenite vein transects harzburgite at a depth of 256 m.

The conventional thermobarometry yielded peak P–T estimates of c. 3.6–4.8 GPa and c. 1030–1150 °C for the garnet peridotites (Medaris et al. 2015). Bulk geochemical signatures of peridotites reflect cryptic to modal metasomatism by a metasomatizing agent derived from subduction environment and containing a significant crustal component. The metasomatism was related to the intrusion of a vein of garnet pyroxenite (Medaris et al. 2015; Čopjaková and Kotková 2018; Kotková et al. 2021a) with major element composition similar to kimberlites (Kotková et al. 2021a). Moreover, reactive infiltration of exsolved residual liquids further into peridotite induced mass exchange between them and the penetrated rocks. This metasomatic process involved entrapment of the liquid pools by newly grown outer zones of the peridotite garnet. Kotková et al. (2021a) estimated the compositions of the metasomatizing media from the modes and compositions of the minerals present in the inclusions. They evolved from more silicic to more carbonate-rich, gradually enriched in LILE (K, Ba) and volatiles (CO_2, Cl) during the infiltration into more distal parts of the peridotite body.

Analytical techniques

A Tescan Mira3GMU FEG-SEM scanning electron microscope (Czech Geological Survey, Prague) equipped with an EDS X-MaxN 80 detector (Oxford Instruments) was utilised for high-resolution BSE imaging of the MSI and phase identification at an accelerating voltage of 15 kV and a beam current of 1.8 nA.

The chemical analyses of the peridotite minerals were obtained using electron probe microanalyzer Cameca SX100 at the Joint Laboratory of Electron Microscopy and Microanalysis (Department of Geological Sciences, Masaryk University and Czech Geological Survey, Brno, Czech Republic). The device was operated in wavelength dispersive mode with acceleration voltage of 15 kV, beam current of 10–20 nA and beam diameter of 1–5 µm. The counting times ranged 10–20 s. The following characteristic spectral lines and natural or synthetic calibration standards were used: SiKα (wollastonite), Ti*K*α (titanite), Al*K*α (almandine), Cr*K*α (chromite), Mg*K*α (pyrope), Ca*K*α (wollastonite), Mn*K*α (spessartine), Fe*K*α (almandine), Ni*K*α (Ni), Na*K*α (albite), K*K*α (sanidine). The matrix effects were corrected using X-Phi routine (Merlet 1994). The specifics of the analysis of the MSI minerals, using the same device, were described by Kotková et al. (2021a).

The mineral abbreviations in the text and figures are used after Warr (2021) as follows: Amp = amphibole, Ap = apatite, Chr = chromite, Cls = celsian (ideally $BaAl_2Si_2O_8$), Cpx = clinopyroxene, Dol = dolomite, Esk = eskolaite (ideally Cr_2O_3), Gn = galena, Gr = graphite, Grt = garnet, Kns = kinoshitalite [ideally $BaMg_3(Al_2Si_2)O_{10}(OH)_2$], Ktp = katophorite [ideally $Na(NaCa)(Mg_4Al)(Si_7Al)O_{22}(OH)_2$], Mgs = magnesite, Mnz = monazite, Nst = norsethite [ideally $CaBa(CO_3)_2$], Ol = olivine, Opx = orthopyroxene, Phl = phlogopite, Pn = pentlandite [ideally $(Fe, Ni)_9S_8$], Prg = pargasite [ideally $NaCa_2(Mg_4Al)(Si_6Al_2)O_{22}(OH)_2$], Sch = scheelite, Spl = spinel, Tho = thorianite (ideally ThO_2).

Sample description and mineral compositions

Host rocks

Garnet peridotite sampled by T-7 borehole includes harzburgite (Hz) and lherzolite (Lh) types. Peridotite samples selected for this study (Hz 322, Hz 276, Lh 332) are characterised by subhedral to anhedral garnet porphyroclasts typically of 5 mm in diameter irregularly distributed within the matrix (Fig. 1a). Ortho- and clinopyroxene occur in two distinct textural types: (i) as relatively rare large porphyroclasts (> 1 mm in diameter), mostly attached to garnet in embayments (Fig. 1a–d) or occurring between two garnet grains, representing an older generation (hereafter referred to as Opx_1 and Cpx_1), (ii) as smaller grains occurring in the equigranular matrix (< 0.3 mm) together with olivine (hereafter referred to as Opx_2 and Cpx_2). Larger clinopyroxene grains of both types contain exsolution lamellae of orthopyroxene (Fig. 1c, d).

Lack of MSI and higher X_{Mg} in pyropic garnet cores (c. 0.83 in both, Hz 276 and Hz 322, respectively) differs from the MSI-bearing outer domains (Fig. 1a), where X_{Mg} drops abruptly to c. 0.78–0.81, with a concomitant drop in Al and increase of Ca and Cr (Fig. 2). Clinopyroxene and orthopyroxene feature relatively uniform X_{Mg} (0.94 and 0.92, respectively). Large Opx_1 (enstatite) grains are somewhat depleted in Al_2O_3 in their cores (c. 0.5 wt. %) compared to their rims (0.7–1.2 wt. %) and relatively homogeneous matrix grains. Large Cpx_1 (diopside) shows increase in Al_2O_3 and Cr_2O_3 from core (c. 0.8 wt. % Al_2O_3, c. 0.7 wt. % Cr_2O_3,) to rim (up to 1.7 wt. % Al_2O_3 and up to 1.1 wt. % Cr_2O_3), whose composition is similar to the matrix grains. Matrix olivine is homogeneous with $X_{Mg} = 0.91$. The representative mineral compositions are shown in Table 1.

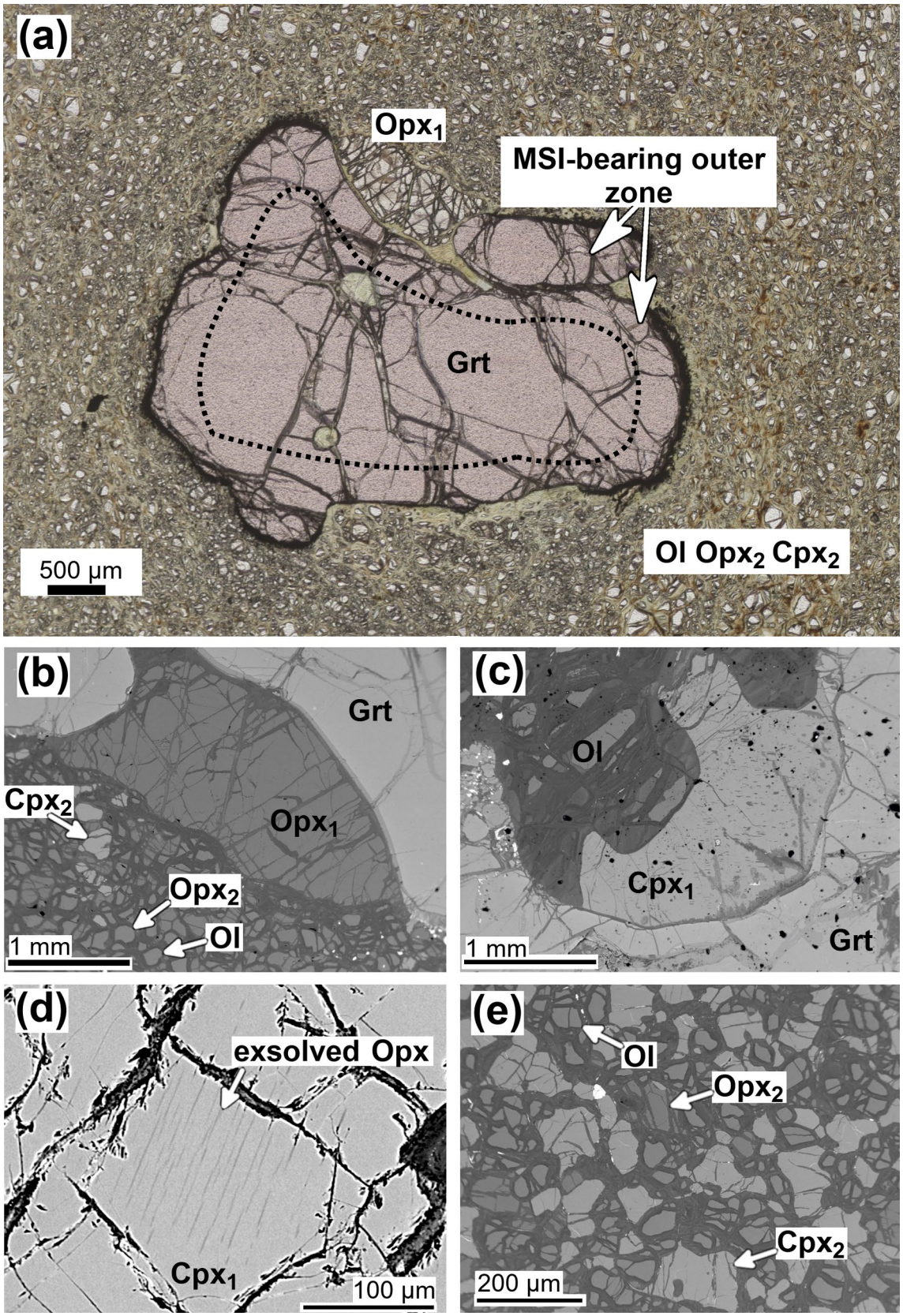
(a)
Opx1
MSI-bearing outer zone
Grt
500 µm
Ol Opx2 Cpx2
(b)
Grt
Cpx2
Opx1
Opx2
Ol
1 mm
(c)
Ol
Cpx1
Grt
1 mm
(d)
exsolved Opx
Cpx1
100 µm
(e)
Ol
Opx2
Cpx2
200 µm

◂**Fig. 1** Image documentation of the investigated harzburgites. **a** A thin-section scan showing Grt and Opx_1 porphyroclasts interpreted to represent remnants of the peak assemblage. The relatively later matrix is composed of Ol, Cpx_2 and Opx_2. **b**–**e** Backscattered electron images depicting the textural relationships, including the distinct textural types of pyroxenes. Larger grains of both, Cpx_1 and Cpx_2 contain exsolved lamellae of Opx (**c**, **d**)

Multiphase solid inclusions

The mineral assemblages of the MSI in the studied samples, textural features and mineral compositions have been described by Čopjaková and Kotková (2018) and Kotková et al. (2021a). The multiphase solid inclusions are concentrated within the 200–1000 µm wide annulus at the rim of garnet porphyroclasts (Fig. 1a) and they reach up to 25 µm and 40 µm in diameter in harzburgite and lherzolite, respectively (Figs. 1, 3, 4). Multiphase solid inclusions from three peridotite samples—Hz 276, Hz 322 and Lh 332—were selected for this study (Fig. 3), as their mineral assemblages are favourable for forward thermodynamic models and conventional thermobarometry. The amount of the MSI relative to the garnet in Lh 332 was estimated to be between 0.07 and 0.37 vol. % (with a weighted average of 0.148 vol. %), depending on the garnet size. Below, the labelling MSI of Hz 276, MSI of Hz 322 and MSI of Lh 322 is used in order to distinguish the minerals occurring in the MSI from the assemblages comprising the host rocks.

Mineral assemblages of the MSI in studied samples are summarised in Table 2. The MSI of Hz 276 contains abundant Amp, and minor Grt. By contrast, the MSI of Hz 322 contains Cpx, whereas Amp is lacking. The fabric can be concentric with barian mica ± other silicates at the rim and dolomite/magnesite in the core (Fig. 3a, d, e, f). The MSI of Lh 332 with the most variable mineral assemblage contains relatively higher Mgs proportions and is commonly characterised by polygonal fabric (Fig. 3b, c; see also Čopjaková and Kotková 2018; Kotková et al. 2021a). Chromite to magnesiochromite is an important carrier of Cr in MSI of harzburgites (Fig. 3a, c). Graphite occurs in some MSI as rounded grains (Fig. 4a) or films along grain boundaries. In addition, graphite can be observed in offshoots or fluid inclusion haloes (Fig. 4b). These decrepitation features are developed at the vicinity of about 30% of the MSI.

The average compositions of the minerals that comprised the MSI were presented by Kotková et al. (2021a). The published compositions, which are used for calculation of the simplified bulk compositions of the MSI (see below) are shown in Table 1 and Supplementary Table S5. In Table 1, we also present unpublished individual point analyses of minerals that coexist within the same MSI in Hz 322. These analyses are used for conventional thermobarometry. Apart from higher $X_{Mg} = 0.84$, pyropic garnet in the MSI differs from pyrope in the host rocks in significantly higher Al_2O_3 (c. 23 wt. %), and lower CaO (< 4 wt. %) and Cr_2O_3 (< 2 wt. %), when compared to about 18 wt. % Al_2O_3, 6% CaO and 6% Cr_2O_3, respectively, in the host garnet porphyroclasts. Amphibole in the MSI corresponds to pargasite; a single analysis with the lowest ^{B}Ca is classified as katophorite. Clinopyroxene composition corresponds to omphacite (4.2–8.6 wt.% Na_2O) and shows $X_{Mg} = 0.92$, which contrasts with diopsidic composition of clinopyroxene in the host rock (< 1.5% Na_2O) and its slightly higher X_{Mg}. Orthopyroxene features elevated Al_2O_3 (> 3 wt. %) and slightly higher X_{Mg} (0.94) compared to Opx_1 and Opx_2 in the host rocks. The composition variables of the measured minerals are projected as markers in the diagrams in Fig. 5.

Relatively few electron microprobe analyses of the minerals comprising MSI, mostly of Hz 322, are appropriate for conventional geothermobarometry (Table 1) due to the very small size of the MSI and their minerals, which results in contamination of the analytical excitation volume by coexisting phases.

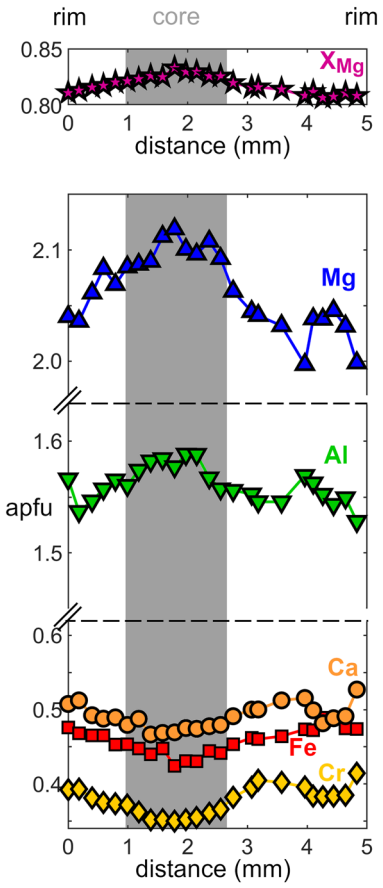

Fig. 2 Compositional profile of garnet porphyroclast from Hz 322 depicting the chemical zoning between the core and the rim

Table 1 Representative chemical compositions of the silicates occurring in the garnet peridotites and their MSI

Mineral	Ol		Ol		Grt		Grt		Grt		Grt	
Sample	Hz 276		Hz 322		Hz 276		Hz 276		Hz 322		Hz 322	
Occurrence	matrix		matrix		porph. C		porph. OZ		porph. C		porph. OZ	
	$n=9$	2σ	$n=2$	2σ	$n=3$	2σ	$n=4$	2σ	$n=3$	2σ	$n=2$	2σ
SiO_2	41.34	0.29	41.32	0.65	41.91	0.69	41.46	0.60	41.63	0.33	41.48	0.16
TiO_2	bdl	0.00	bdl	0.01	0.16	0.03	0.18	0.05	0.16	0.01	0.17	0.03
Al_2O_3	bdl	0.00	bdl	0.02	18.56	0.32	18.16	0.36	18.50	0.05	18.03	0.21
Cr_2O_3	bdl	0.00	bdl	0.00	5.97	0.26	6.31	0.21	6.13	0.07	6.66	0.01
MgO	49.76	0.11	50.11	1.15	19.72	0.22	19.04	0.29	19.43	0.32	18.80	0.04
CaO	bdl	0.00	bdl	0.00	6.03	0.05	6.29	0.45	6.08	0.05	6.22	0.10
MnO	0.12	0.03	0.11	0.03	0.31	0.03	0.36	0.05	0.30	0.06	0.39	0.01
FeO	8.79	0.28	8.30	0.15	7.31	0.13	7.97	0.12	7.05	0.09	8.02	0.06
NiO	0.45	0.02	0.41	0.12	bdl	0.00	bdl	0.00	bdl	0.00	bdl	0.00
Na_2O	bdl	0.00	bdl	0.00	bdl	0.00	bdl	0.00	bdl	0.00	0.02	0.04
K_2O	bdl	0.00	bdl	0.00	bdl	0.00	bdl	0.00	bdl	0.00	bdl	0.00
Total	100.44	0.04	100.25	1.34	99.97	0.23	99.77	1.17	99.28	0.43	99.77	0.15
Si	1.004	0.007	1.003	0.016	3.026	0.050	3.017	0.044	3.025	0.024	3.022	0.012
Ti	0.000	0.000	0.000	0.000	0.009	0.002	0.010	0.003	0.008	0.001	0.010	0.002
Al	0.000	0.000	0.000	0.000	1.579	0.028	1.558	0.031	1.585	0.005	1.548	0.018
Cr	0.000	0.000	0.000	0.000	0.341	0.015	0.363	0.012	0.353	0.004	0.383	0.001
Mg	1.802	0.004	1.814	0.041	2.123	0.024	2.066	0.031	2.106	0.035	2.042	0.005
Ca	0.000	0.000	0.000	0.000	0.467	0.004	0.490	0.035	0.473	0.004	0.485	0.008
Mn	0.002	0.001	0.002	0.001	0.019	0.002	0.022	0.003	0.019	0.003	0.024	0.001
Fe	0.179	0.006	0.169	0.003	0.442	0.008	0.485	0.007	0.429	0.005	0.488	0.003
Ni	0.009	0.000	0.008	0.002	0.000	0.000	0.000	0.000	0.000	0.000	0.000	0.000
Na	0.000	0.000	0.000	0.000	0.000	0.000	0.000	0.000	0.000	0.000	0.003	0.005
K	0.000	0.000	0.000	0.000	0.000	0.000	0.000	0.000	0.000	0.000	0.000	0.000
cat sum	2.996		2.997		8.005		8.012		7.997		8.003	
O	4.000		4.000		12.000		12.000		12.000		12.000	
Mineral	Grt[a]		Grt	Grt[a]	Opx		Opx		Opx		Opx	
Sample	Hz 276		Hz 322	Lh 332	Hz 276		Hz 276		Hz 322		Hz 322	
Occurrence	MSI		MSI	MSI	porph. C		matrix		porph. C		matrix	
	$n=4$	2σ	$n=1$	$n=1$	$n=4$	2σ	$n=2$	2σ	$n=3$	2σ	$n=7$	2σ
SiO_2	42.72	1.16	43.56	42.35	57.94	0.49	57.51	0.03	58.02	0.53	57.97	0.34
TiO_2	0.00	0.01	bdl	bdl	bdl	0.00	bdl	0.00	bdl	0.00	bdl	0.00
Al_2O_3	22.82	0.37	22.86	23.65	0.53	0.08	1.09	0.03	0.63	0.14	0.77	0.15
Cr_2O_3	1.67	0.48	1.93	0.76	0.29	0.02	0.36	0.02	0.33	0.09	0.31	0.09
MgO	21.62	0.51	21.47	21.94	35.65	0.48	34.78	0.27	35.47	0.94	35.42	0.67
CaO	2.89	0.53	3.71	2.93	0.57	0.20	0.44	0.01	0.52	0.05	0.41	0.17
MnO	0.41	0.12	0.39	0.35	0.13	0.05	0.14	0.07	0.12	0.02	0.12	0.04
FeO	8.02	0.73	7.26	8.17	5.30	0.35	5.86	0.00	5.41	0.14	5.45	0.24
NiO	bdl	0.00	bdl	bdl	0.09	0.13	0.07	0.01	0.15	0.07	0.08	0.05
Na_2O	bdl	0.00	bdl	0.03	bdl	0.00	bdl	0.00	bdl	0.00	bdl	0.00
K_2O	bdl	0.00	bdl	bdl	bdl	0.00	bdl	0.00	bdl	0.00	bdl	0.00
Total	100.21	1.38	101.18	100.30	100.49	0.94	100.25	0.21	100.66	0.69	100.55	0.74
Si	3.014	0.038	3.036	2.991	1.981	0.017	1.974	0.001	1.981	0.018	1.980	0.012
Ti	0.000	0.000	0.000	0.015	0.000	0.000	0.000	0.000	0.000	0.000	0.000	0.000
Al	1.898	0.024	1.877	1.784	0.021	0.003	0.044	0.001	0.025	0.006	0.031	0.006
Cr	0.093	0.027	0.106	0.138	0.008	0.000	0.010	0.000	0.009	0.002	0.008	0.002
Mg	2.274	0.030	2.230	2.144	1.817	0.024	1.780	0.014	1.805	0.048	1.804	0.034
Ca	0.218	0.042	0.277	0.364	0.021	0.007	0.016	0.001	0.019	0.002	0.015	0.006
Mn	0.025	0.007	0.023	0.021	0.004	0.002	0.004	0.002	0.004	0.000	0.003	0.001
Fe	0.473	0.055	0.423	0.535	0.152	0.010	0.168	0.000	0.155	0.004	0.156	0.007

Table 1 (continued)

Mineral	Grt[a]		Grt	Grt[a]	Opx		Opx		Opx		Opx	
Sample	Hz 276		Hz 322	Lh 332	Hz 276		Hz 276		Hz 322		Hz 322	
Occurrence	MSI		MSI	MSI	porph. C		matrix		porph. C		matrix	
	$n=4$	2σ	$n=1$	$n=1$	$n=4$	2σ	$n=2$	2σ	$n=3$	2σ	$n=7$	2σ
Ni	0.000	0.000	0.000	0.000	0.002	0.004	0.002	0.000	0.004	0.002	0.002	0.001
Na	0.000	0.000	0.000	0.005	0.000	0.000	0.000	0.000	0.000	0.000	0.000	0.000
K	0.000	0.000	0.000	0.000	0.000	0.000	0.000	0.000	0.000	0.000	0.000	0.000
cat sum	7.999		7.972	7.997	4.005		3.999		4.002		4.000	
O	12.000		12.000	12.000	6.000		6.000		6.000		6.000	

Mineral	Opx[a]	Opx	Cpx		Cpx		Cpx		Cpx		Cpx	Cpx[a]	
Sample	Hz 276	Hz 322	Hz 276		Hz 276		Hz 322		Hz 322		Hz 322	Lh 332	
Occurrence	MSI	MSI	porph. C		matrix		porph. C		matrix		MSI	MSI	
	$n=1$	$n=1$	$n=2$	2σ	$n=2$	2σ	$n=4$	2σ	$n=11$	2σ	$n=1$	$n=3$	2σ
SiO_2	58.10	55.42	54.84	0.29	54.58	1.19	54.58	0.79	54.35	0.56	53.49	54.19	0.46
TiO_2	bdl	0.04	bdl	0.00	bdl	0.00	0.06	0.05	0.03	0.04	0.07	0.03	0.01
Al_2O_3	1.47	3.21	0.82	0.07	1.40	0.13	1.03	0.55	1.22	0.34	9.32	10.15	1.74
Cr_2O_3	0.54	1.02	0.75	0.01	1.00	0.05	0.98	0.13	0.96	0.14	3.50	2.24	0.76
MgO	36.03	34.29	17.77	0.30	17.16	0.08	17.52	1.21	17.49	0.50	11.39	10.68	0.09
CaO	0.67	0.38	22.93	0.25	23.15	0.03	23.70	0.37	23.79	0.42	14.09	15.25	1.25
MnO	0.08	0.06	0.09	0.06	0.08	0.04	0.06	0.06	bdl	0.00	0.08	0.05	0.05
FeO	3.18	3.86	2.17	0.08	2.01	0.03	1.91	0.17	1.82	0.09	1.85	1.76	0.38
NiO	bdl	bdl	0.06	0.05	bdl	0.00	bdl	0.00	bdl	0.00	bdl	bdl	0.00
Na_2O	bdl	0.08	0.62	0.01	0.81	0.22	0.62	0.24	0.70	0.15	5.67	5.83	0.75
K_2O	bdl	0.13	bdl	0.00	bdl	0.00	bdl	0.00	bdl	0.00	bdl	0.03	0.02
Total	100.20	98.49	100.06	0.24	100.19	1.34	100.45	1.85	100.36	0.72	99.46	100.33	0.61
Si	1.974	1.925	1.987	0.010	1.976	0.043	1.973	0.028	1.967	0.020	1.923	1.917	0.035
Ti	0.000	0.001	0.000	0.000	0.000	0.000	0.002	0.001	0.001	0.001	0.002	0.000	0.001
Al	0.059	0.131	0.035	0.003	0.060	0.006	0.044	0.023	0.052	0.015	0.395	0.423	0.067
Cr	0.014	0.028	0.022	0.000	0.029	0.001	0.028	0.004	0.027	0.004	0.100	0.063	0.022
Mg	1.825	1.776	0.960	0.016	0.926	0.005	0.944	0.065	0.943	0.027	0.610	0.563	0.011
Ca	0.025	0.014	0.890	0.010	0.898	0.001	0.918	0.014	0.922	0.016	0.543	0.578	0.054
Mn	0.002	0.002	0.003	0.002	0.002	0.001	0.002	0.002	0.000	0.000	0.002	0.001	0.002
Fe	0.090	0.112	0.066	0.002	0.061	0.001	0.058	0.005	0.055	0.003	0.056	0.079	0.063
Ni	0.000	0.000	0.002	0.002	0.000	0.000	0.000	0.000	0.000	0.000	0.000	0.000	0.000
Na	0.000	0.006	0.044	0.001	0.057	0.016	0.043	0.017	0.049	0.011	0.395	0.400	0.047
K	0.000	0.006	0.000	0.000	0.000	0.000	0.000	0.000	0.000	0.000	0.000	0.001	0.002
cat sum	3.989	4.000	4.007		4.009		4.011		4.017		4.026	4.025	
O	6.000	6.000	6.000		6.000		6.000		6.000		6.000	6.000	

Mineral	Amp[a]		Amp[a]	
Sample	Hz 276		Lh 332	
Occurrence	MSI		MSI	
	$n=8$	2σ	$n=8$	2σ
SiO_2	45.87	2.51	44.06	1.41
TiO_2	0.02	0.03	0.09	0.05
Al_2O_3	12.67	2.20	16.63	1.60
Cr_2O_3	3.02	0.78	2.08	0.65
Fe_2O_3*	0.70	0.58	1.12	0.89
FeO	0.98	0.53	1.05	0.75
MnO	0.02	0.02	0.03	0.03
MgO	18.71	0.94	17.45	1.19
NiO	0.05	0.09	0.01	0.03

Table 1 (continued)

	Mineral	Amp[a]		Amp[a]	
	Sample	Hz 276		Lh 332	
	Occurrence	MSI		MSI	
		$n=8$	2σ	$n=8$	2σ
	BaO	0.32	0.14	0.64	0.26
	SrO	0.08	0.12	0.01	0.02
	CaO	12.18	0.45	10.33	1.42
	K_2O	0.36	0.11	0.39	0.23
	Na_2O	2.72	0.35	4.56	0.76
	Cl	0.26	0.11	0.44	0.60
	F	0.12	0.04	0.12	0.05
	H_2O*	2.01	0.05	1.95	0.18
	O = $^{-}$F,Cl	− 0.11		− 0.15	
	Total	99.71	1.45	100.23	1.28
T-site	Si	6.460	0.299	6.178	0.151
	Al	1.540	0.299	1.822	0.151
C-site	Ti	0.002	0.004	0.010	0.006
	Al	0.564	0.081	0.926	0.178
	Cr	0.337	0.088	0.230	0.071
	Fe^{3+}	0.074	0.062	0.118	0.094
	Fe^{2+}	0.085	0.088	0.065	0.124
	Mg	3.927	0.176	3.644	0.220
	Ni	0.005	0.011	0.002	0.004
B-site	Mn^{2+}	0.002	0.002	0.003	0.003
	Fe^{2+}	0.031	0.032	0.059	0.064
	Mg	0.000	0.000	0.002	0.010
	Ca	1.838	0.087	1.552	0.198
	Sr	0.006	0.010	0.000	0.001
	Ba	0.018	0.008	0.035	0.014
	Na	0.122	0.079	0.383	0.174
A-site	Na	0.620	0.117	0.858	0.068
	K	0.064	0.019	0.070	0.041
W-site	OH	1.883	0.042	1.823	0.164
	F	0.051	0.018	0.053	0.021
	Cl	0.061	0.024	0.104	0.145
	O	0.004	0.007	0.020	0.011

porph. = porphyroclast, C = core, OZ = outer MSI-bearing zone of garnet, bdl = below the detection limit

The chemical compositions are presented as oxide wt. %

Crystal-chemical formulae of olivine, garnet and pyroxenes were calculated based on 4, 12 and 6 oxygens, respectively, and are presented as atoms per formula unit

All iron in olivine, garnet and pyroxenes is considered as Fe^{2+}

Amphibole formulae are based on 24 (O, OH, F, Cl) anions. The Fe^{2+}/Fe^{3+} ratio was calculated using cation normalisation scheme T + C + B = 15 to keep the formula electro-neutral. H_2O* is calculated based on stoichiometry

[a]Average compositions of the MSI phases were published in Kotková et al. (2021a)

Conventional thermobarometry

Host rocks

In order to evaluate the P–T evolution of the rocks prior to the crystallisation of the MSI, we estimated the P–T conditions of the peak, and of MSI entrapment in the studied harzburgites samples (Table 3). The Al-depleted cores of large Opx_1, Al- and Cr- depleted cores of large clinopyroxene (Cpx_1), and garnet cores with the highest X_{Mg} were used to calculate the peak P–T conditions. The estimates of the entrapment conditions employ the composition of the MSI-bearing garnet domain with a lower X_{Mg} combined with the matrix pyroxene (Opx_2 and Cpx_2) compositions, which are

similar to the rims of large Opx_1 and Cpx_1. To evaluate the upper pressure limit of the entrapment, the same garnet composition is coupled with the large pyroxene cores used for constraint of the peak.

The new pressure–temperature estimates constraining the evolution of garnet harzburgites were obtained using several conventional geothermometers and geobarometers. The pressure estimates are based on Al content in orthopyroxene (Nickel and Green 1985; Brey and Köhler 1990) and Cr content in clinopyroxene (Nimis and Taylor 2000), both coexisting with garnet. The temperatures were calculated using the distribution of Mg and Fe between garnet and olivine (O'Neil and Wood 1979; Wu and Zhao 2007), garnet and clinopyroxene (Powell 1985) and garnet and orthopyroxene (Harley 1984) and two-pyroxene solvus equilibria (Bertrand and Mercier 1985; Brey and Köhler 1990), respectively.

The peak P–T conditions were constrained by the intersections of the equilibrium curves for Al-in-Opx barometer and garnet-pyroxene thermometers between c. 1060–1120 °C and 5.1–5.7 GPa in the case of Hz 276, and 990–1150 °C and 4.4–5.6 GPa in the case of Hz 322. Garnet-olivine thermometry yields comparable and higher temperatures for Hz 322 and Hz 276 (1110–1150 °C and 1160–1190 °C at a reference pressure of 5 GPa, respectively). Two-pyroxene thermometers yield significantly lower temperatures and thus also lower pressures. The equilibria intersect at c. 870–910 °C at 4.4–4.6 GPa in the case of Hz 276, and at even lower temperatures of up to 780 °C in the case of Hz 322.

The conditions of the MSI entrapment calculated for the matrix pyroxenes and MSI-bearing garnet domains are constrained by the intersection of the Mg–Fe exchange equilibria and Al-in-Opx and Cr-in-Cpx equilibria between c. 940–1050 °C at 3.6–4 GPa in the case of Hz 276 and 900–1000 °C at 3.9–4.4 GPa in the case of Hz 322. Al-in-Opx barometry employing large pyroxene cores yield results comparable to those obtained for the peak. However, the drop of X_{Mg} in the outer part of garnet compared to the core gives somewhat lower garnet–pyroxene temperatures: 990–1010 °C at 4.7–5.1 GPa in the case of Hz 276 and 970–995 °C at 4.2–4.8 GPa in the case of Hz 322.

Multiphase solid inclusions

Conventional thermobarometry was applied to two multiphase solid inclusions of Hz 322, for which appropriate analyses of co-existing clinopyroxene, orthopyroxene and garnet were obtained (Tables 1, 3). The two-pyroxene solvus thermometer (Nickel and Green 1985; Brey and Kohler 1990), garnet–clinopyroxene thermometer (Powell 1985), Al-in-Opx barometer (Bertrand and Mercier 1985; Brey and Kohler 1990) as well as Cr-in-Cpx barometer (Nimis and Taylor 2000) intersect at a reasonably narrow P–T region of c. 900–1070 °C/2–2.8 GPa. Garnet–orthopyroxene thermometry yielded lower temperature, c. 800 °C at a reference pressure of 2.5 GPa.

Forward thermodynamic modelling of the MSI assemblages

Modelling strategy, limitations and considerations

Despite the significant progress in developing thermodynamic models of melts of a wide range of crustal and mantle compositions including melting of mantle peridotites (Jennings and Holland 2015; Holland et al. 2018), the thermodynamic model appropriate for a carbonate–silicate (COH-bearing) melt is lacking. Thus, the conditions at which the trapped melt inclusions crystallised into solids can only be estimated based on a comparison with appropriate melting experiments (see below). Despite that, we conducted forward thermodynamic modelling in order to evaluate, whether the mineral assemblages observed in the MSI coexisted in equilibrium and to estimate the corresponding physico-chemical conditions. It needs to be emphasised, that only the stability fields below the solidus (whose position is uncertain) are valid, whereas those above the solidus are metastable with respect to a melt or a partially molten assemblage. Therefore, suprasolidus conditions were approximated by those relevant for carbonated and hydrated Hawaiian pyrolite (Wallace and Green 1988). The melt stability field is projected in the P–T pseudosections (Fig. 6a, d, g) using a dot hatch pattern.

The average bulk compositions of the distinct types of MSI were previously estimated based on the average proportions and compositions of the constituent minerals from Hz 322, Hz 276 and Lh 332, respectively, using mineral proportions from 9–12 inclusions in each sample (Kotková et al. 2021a). The approach is described by the cited authors in detail (see their Fig. 2). For the purposes of the forward thermodynamic modelling, the average bulk compositions had to be simplified. Contributions from amphibole, dolomite, magnesite, pyroxenes, garnet and chromite to the bulk compositions were considered. On the contrary, the contributions of certain phases to the bulk composition had to be neglected in the thermodynamic models. The neglected phases include phosphates (apatite, monazite), sulphides (pentlandite, galena, chalcopyrite), U-Th oxides (thorianite, uraninite), celsian (barian feldspar) and norsethite (barian analogue of dolomite). The specific treatment of the barian mica is described below. The complete simplification procedure is described in detail in the Supplementary Document 1. The supplementary figures and tables in this document are referred to as Tables S1–S4 and Figures S1–S4.

The observed minerals crystallised from a former relatively homogeneous (on a sample scale) media and the

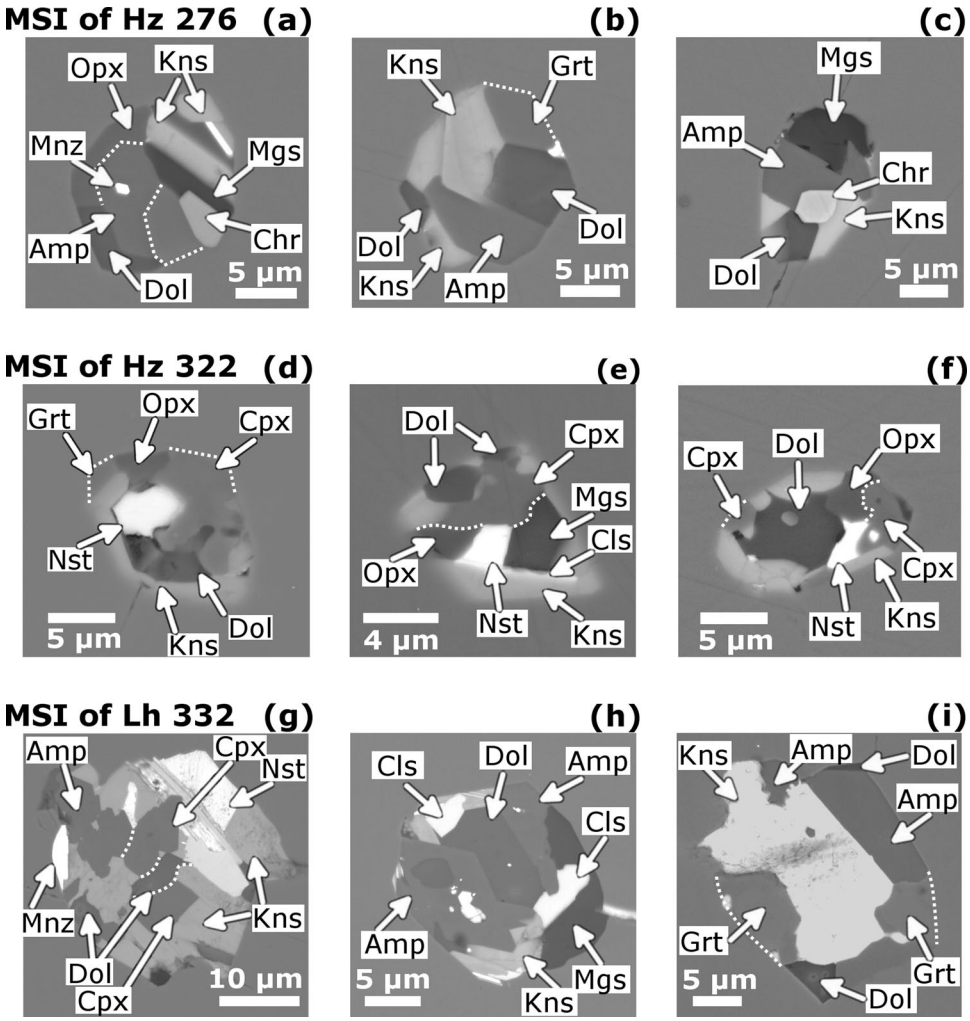

Fig. 3 Backscattered electron images of the MSI. All MSI are enclosed in garnets. Some MSI exhibit distinct concentric (**d**, **f**, **h**) or polygonal (**b**, **c**) textures. The carbonate–silicate assemblages appropriate for the thermodynamic models include *Kns/Phl Dol Amp Opx Grt Mgs* in the case of Hz 276 (**a**–**c**), *Kns/Phl Dol Cpx Opx Mgs Grt Chr* in the case of Hz 322 (**d**–**f**), and *Kns/Phl Amp Dol Mgs Cpx*$\pm$*Grt* in the case of Lh 332 (g–**i**), respectively

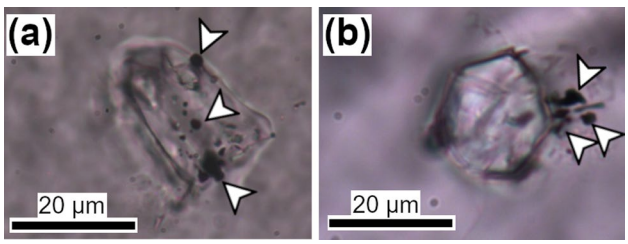

Fig. 4 Photomicrographs of graphite (marked with arrows) occurring within the MSI and the adjacent decrepitation features (offshoots)

mineral proportions in distinct sections are thus assumed to follow a normal distribution, as per statistical considerations. Therefore, the averaging of the individual bulk compositions of the sampled MSI, as employed by the Kotková et al. (2021a), is expected to converge towards the representative average composition of the original melts. Nevertheless, the estimated uncertainties in the mineral modes (and consequently in the estimated bulk compositions) are significant due to the inclusion heterogeneity and the limited number of reintegrated MSI. For example, in case of MSI of Hz 322, the standard deviations of the modes of the relatively more abundant minerals (dolomite, clinopyroxene, and orthopyroxene) range between 33 and 42% relative, and those of the minor minerals (magnesite, garnet and chromite) are as high as 105–155% relative (Table S2). Thus, we investigated the extent to which these uncertainties in the bulk

Table 2 Mineral assemblages occurring in the MSI and the relative abundances of the minerals

Sample	Major minerals	Minor minerals	Accessory minerals
MSI of Hz 276	Amp = Kns = Dol	Grt	Mgs, Opx, Cls, Mnz, Pn
MSI of Hz 322	Kns > Dol > Cpx	Cls, Opx, Mgs	Grt, Mnz, Chr, Sch, Nst
MSI of Lh 332	Kns = Amp > Dol > Mgs = Nrs	Cpx	Grt, Cls, Tho, Mnz, Ap, Pn, Gn

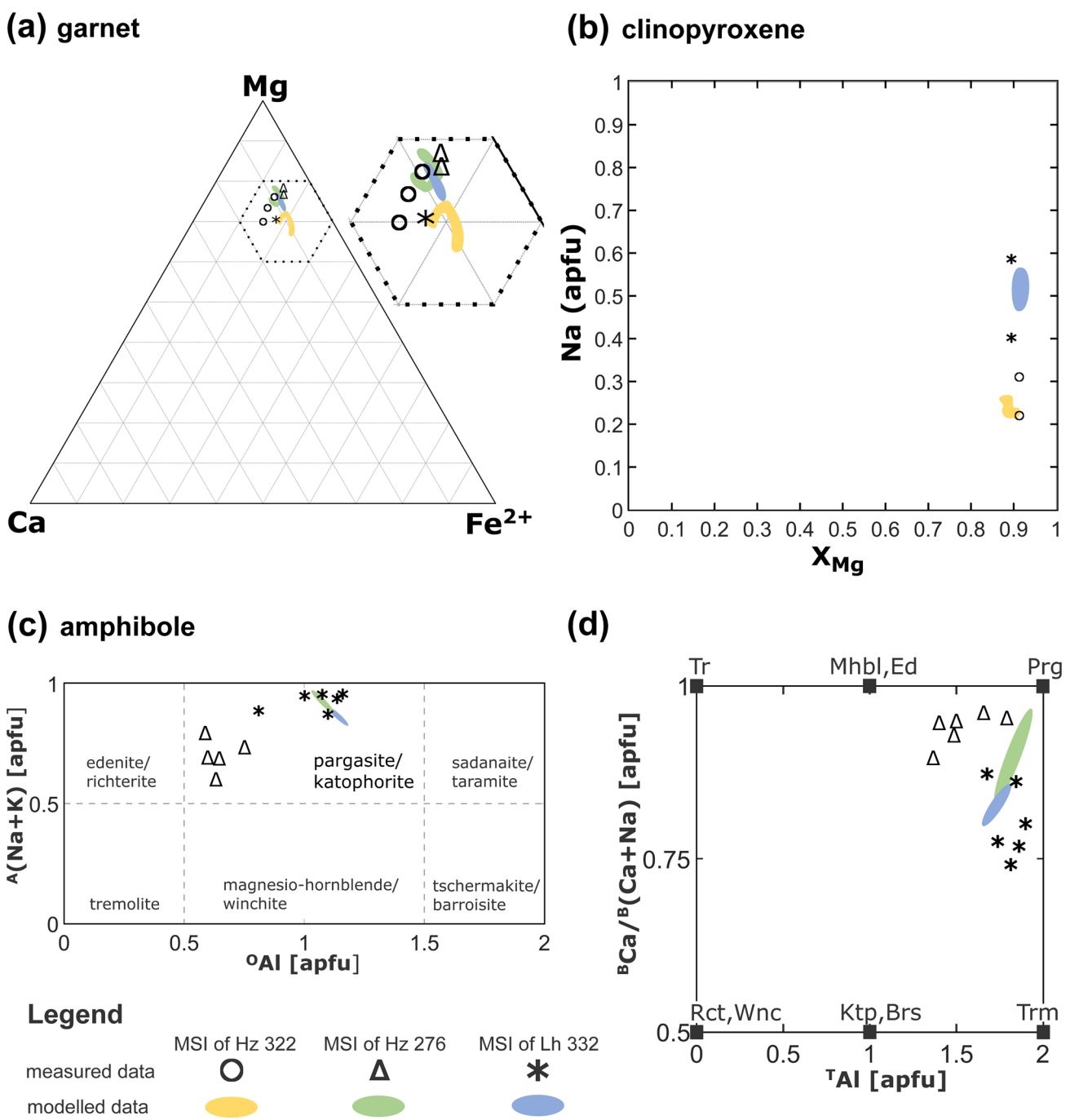

Fig. 5 Ternary and binary plots demonstrating the measured (black markers) and modelled (shaded areas) composition parameters in the solid solutions occurring in the MSI—garnet (**a**), clinopyroxene (**b**), and amphibole (**c**, **d**)

composition, arising from the MSI heterogeneity, propagate to the stability limits of the mineral assemblage of interest in the thermodynamic models. This verification procedure was conducted using the mineral assemblage in MSI of Hz 322 because this sample provides the most robust and straightforward estimate of the physico-chemical conditions of the (re)-equilibration, as discussed below. A Monte Carlo-type simulation was performed to generate 10 reference sets of random bulk compositions utilising the average values and uncertainties calculated for the mineral proportions in MSI of Hz 322 (see Supplementary Document 1 for the details of the approach and Tables S2 and S3 for the associated data). This approach to evaluating the uncertainties in the stability limits is similar to the one described by Palin et al. (2016),

Table 3 Pressure–temperature estimates for the specific stages of the evolution of the garnet peridotites and their MSI

Stage of the rock evolution		Peak conditions		Melt entrapment		MSI (re)-equilibration
Sample		Hz 322	Hz 276	Hz 322	Hz 276	MSI of Hz 322
Reference pressure (GPa)		5	5	4.5	4.5	2.5
Thermometric method	Calibration					
Grt-Ol	O'Neil and Wood (1979)	1108	1160	934	1017	
Grt-Ol	Wu and Zhao (2007)	1147	1191	1006	1071	
Grt-Cpx	Powell (1985)	1014	1052	917	970	1096
Grt-Opx	Harley (1984)	1115	1079	983	1055	818
two Px	Bertrand and Mercier (1985)	712	869	780	876	954
two Px	Brey and Köhler (1990)	783	925	721	811	1005
Reference temperature (°C)		1050	1050	1000	1000	1000
Barometric method						
Al-in-Opx	Nickel and Green (1985)	5.09	5.33	4.40	3.79	2.50
Al-in-Opx	Brey and Köhler (1990)	4.94	5.20	4.00	3.34	2.33
Cr-in-Cpx	Nimis and Taylor (2000)	4.55	5.10	4.17	4.90	2.37

although the cited authors used arbitrary uncertainties (2σ of 10% and 20% relative) for generating their testing datasets.

Trioctahedral barian mica (3.5–18.5 wt. % BaO) which occurs as a major phase (≥ 30 vol. %) in all MSI, poses challenges for the modelling. The mica is a solid solution of phlogopite, kinoshitalite and ferrokinoshitalite, with phlogopite content ranging between c. 30 and 73 mol. % in the samples of interest (Čopjaková and Kotková 2018). Thus, the phlogopite component is the predominating carrier of potassium (incorporating c. 80–100% of the element budget in the system, with only a minor fraction being incorporated in amphibole—see data of Kotková et al. 2021a). Phlogopite is known to be stable in K-enriched ultrabasic mantle rocks (e.g. Modreski and Boettcher 1973; Thibault et al. 1992; Fumagalli et al. 2009; Tumiati et al. 2013) and can be used as a representative of trioctahedral mica in the models. The presence of phlogopite in the thermodynamic models is crucial for evaluating the stability limits of the amphibole-free assemblages in the composition space involving H_2O, particularly in the case of MSI of Hz 322, where trioctahedral mica is the only hydrous phase present. Furthermore, it is expected to affect the composition of amphibole, which is the other K-bearing phase in MSI of Hz 276 and Lh 332. Preliminary models were calculated with phlogopite as a saturated component, whose thermodynamic activity was set to unity. Consequently, the software AX, namely the version AX62 updated in 2022 (https://filedn.com/lU1GlyFhv3UuXg5E9dbnWFF/TJBHpages/ax.html), developed by Tim Holland employing biotite mixing model of Powell and Holland (1999) with ideal activity expression $4X_{K,A}X_{Mg,M1}X^{2}_{Mg,M3}X_{Al,T1}X_{Si,T1}$ was used to estimate the thermodynamic activities of the phlogopite component in the barian mica compositions, as reported by Čopjaková and Kotková (2018). These estimates calculated at reference conditions of 1000 °C and 2 GPa (based on the preliminary models) provided phlogopite activities of 0.117 and 0.122 for MSI of Hz 276 and Lh 332, respectively. The values are assumed to be rough estimates because the mixing behaviour of barian components in the trioctahedral mica are unknown, thus not considered in the KFMASH mixing model.

Input parameters of the thermodynamic models

The models were constructed using Perple_X 6.9.0 (Connolly 2005, 2009). Thermodynamic dataset by Holland and Powell (2011), activity–composition expressions for carbonates (Franzolin et al. 2011), amphibole and clinopyroxene (Green et al. 2016), orthopyroxene, garnet, olivine, spinelides (Jennings and Holland 2015) and the compensated Redlich–Kwong equation of state for H_2O-CO_2 fluid (Holland and Powell 1991) were used.

The simplified bulk compositions used for the modelling include Na_2O, CaO, FeO, MgO, Al_2O_3 and SiO_2 as constrained system components, with their contents explicitly defined (Table 4). Chromium oxide was included in the case of amphibole-free and chromite-bearing MSI of Hz 322 only. The other samples contain amphibole as a dominant carrier of chromium, however, incorporation of Cr in amphibole cannot be simulated by the models. To investigate the impact of the decreased phlogopite activity, the refined models were recalculated with phlogopite activities of 0.1, 0.2, and 0.3, respectively. Below (Fig. 6), we present the phase diagrams calculated with phlogopite activity of 0.1; the models with activity equal to unity are attached as Figures S3 and S4.

The modelled assemblages of interest were as follows:

- *Phl Dol Cpx Opx Mgs Grt Chr* in MSI of Hz 322

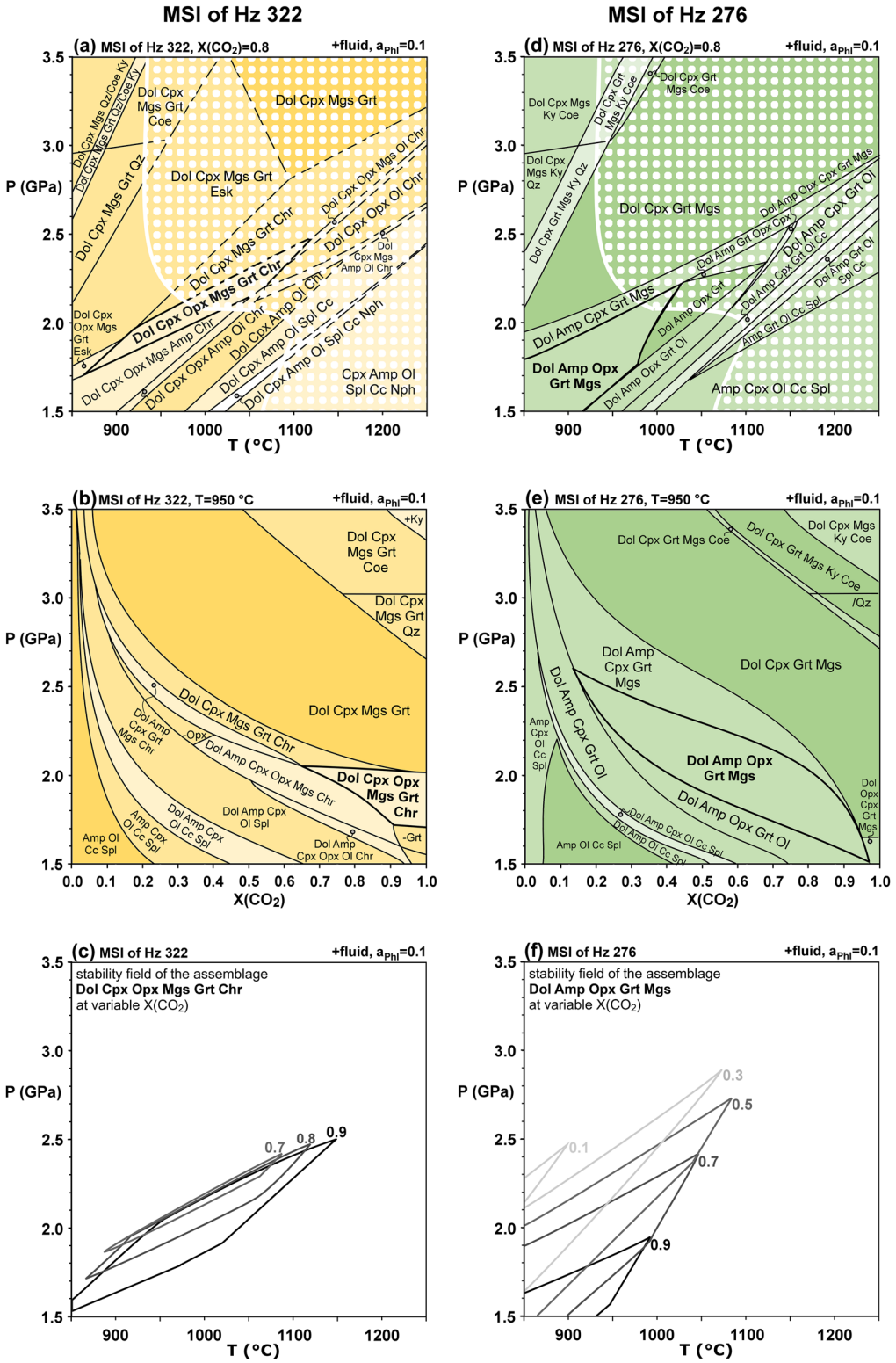

Fig. 6 Forward thermodynamic models reproducing the MSI assemblages from Hz 322 (**a**–**c**), Hz 276 (**d**–**f**) and Lh 332 (**g**–**i**), respectively. The carbonate–silicate assemblages of interest are labelled in bold and their stability fields bounded using the bold solid lines. The modelled assemblages are saturated with a CO_2–H_2O fluid (see text and Fig. 7 for explanation). The thermodynamic activity of phlogopite is fixed at 0.1. The stability fields above the solidus are indeed metastable with respect to partially molten assemblages. Suprasolidus conditions relevant for carbonated and hydrated Hawaiian pyrolite (Wallace and Green 1988) are projected in the P–T pseudosections (**a**, **d**, **g**) using a dot hatch pattern

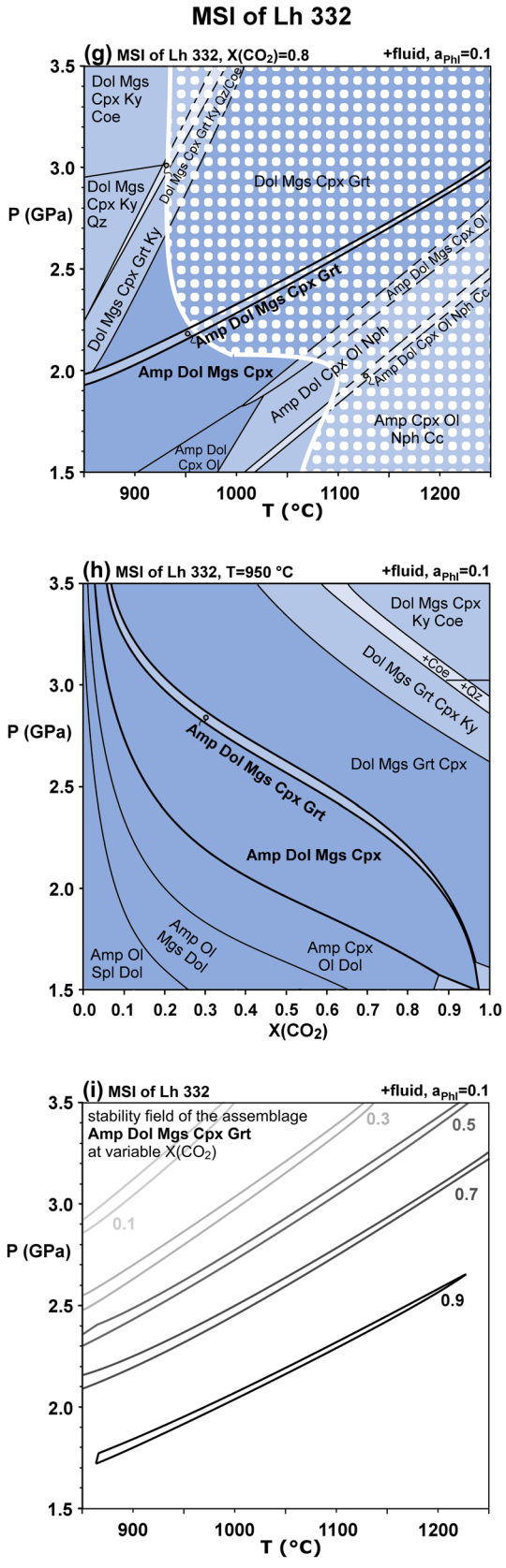

Fig. 6 (continued)

- *Phl Dol Amp Opx Grt Mgs* in MSI of Hz 276
- *Phl Amp Dol Mgs Cpx Grt* in MSI of Lh 332

The P–T window considered in the models was chosen based on the results of the conventional thermobarometry. Significant amounts of H_2O and CO_2 stored in the minerals arise a question of the co-existence of a fluid phase to stabilise them, and if so, what was the composition of the fluid. To challenge this issue, the following approach to the forward modelling was adopted: (1) P–T pseudosections of the fluid-saturated assemblages in the P–T range of 850–1250 °C, 1.5–3.5 GPa at variable values of $X(CO_2)$ in the associated CO_2–H_2O fluid (Fig. 6a, d, g) were constructed, and (2) P-$X(CO_2)$ pseudosections at a fixed temperature of 950 °C were constructed (Fig. 6b, e, h) to investigate stability limits of the observed assemblages. Furthermore, (3) the influence of fluid undersaturation on the stability of the assemblages of interest was investigated. For this purpose, ternary diagrams at fixed P and T were modelled with vertexes representing bulk composition of the MSI (i) without CO_2 and H_2O, (ii) with 40 mol. % H_2O, (iii) with 40 mol.% CO_2 (Fig. 7). Obviously, this approach involves indirect specification of the chemical potentials of CO_2 and H_2O, as well as their amounts incorporated in the solid phases, which are constrained based on the composition of the saturated fluid phase in the models specified in (1) and (2).

Topology of modelled pseudosections and stability fields of the observed assemblages

The constructed thermodynamic models successfully reproduce all the observed mineral assemblages under specific P–T–$X(CO_2)$ conditions (see the labels in bold in Fig. 6). The observed and the modelled mineral modes, as well as the contents of CO_2 and H_2O stored in dolomite, amphibole, and magnesite show perfect agreement (Table 4). The stability fields of the MSI assemblages of interest are mostly narrow extending from lower to higher P–T conditions for a particular $X(CO_2)$ value.

The MSI of Hz 322 is represented by mineral assemblage *Dol Cpx Opx Mgs Grt Chr*. It is obvious from the P-$X(CO_2)$ diagram and P–T diagram depicting the stability field of the assemblage as a function of $X(CO_2)$ (Fig. 6b, c) that these minerals may co-exist only at relatively high $X(CO_2) \geq 0.7$. Whereas the low-pressure boundary of this field (c. 1.7–2.1 GPa at the reference temperature of 950 °C), characterised by appearance of amphibole or disappearance of garnet, is somewhat sensitive to the exact $X(CO_2)$ value, the high-pressure boundary (c. 2.2 GPa), marked by the breakdown of orthopyroxene, is very insensitive to the composition of the coexisting fluid phase.

Table 4 Compositional parameters of the thermodynamic models and comparison of the observed and modelled mineral modes

Sample	Observed mineral modes (vol. %)[a]	Simplified bulk compositions of the considered MSI assemblages[a,b] (wt. %)	Modelled mineral modes (vol. %)[a,c]	Modelled CO_2 and H_2O contents in Amp, Dol, Mgs[c]
MSI of Hz 322	Dol 55.3, Cpx 27.4, Opx 9.8, Mgs 5.2, Grt 1.8, Chr 0.3	SiO_2 19.83, Al_2O_3 2.54, Cr_2O_3 1.21, MgO 21.52, CaO 21.26, FeO 2.48, Na_2O 1.01, CO_2 29.65	Dol 54–58, Cpx 26–28, Opx < 10, Mgs 6–12, Grt 2–4, Chr < 1	CO_2 29.85 wt. %
MSI of Hz 276	Amp 45.5, Dol 33, Grt 15.2, Mgs 3.9, Opx 1.7	SiO_2 29.84, Al_2O_3 10.44, MgO 20.94, CaO 14.77, FeO 3.12, Na_2O 1.29, CO_2 15.71, H_2O 0.91	Amp 38–46, Dol 36–38, Grt < 12, Mgs 2–10, Opx < 12	CO_2 18.79 wt. %, H_2O 0.73 wt. %
MSI of Lh 332	Amp 48.7, Dol 26.5, Mgs 11.3, Cpx 11, Grt 2.5	SiO_2 28.70, Al_2O_3 10.38, MgO 20.56, CaO 14.09, FeO 2.56, Na_2O 2.91, CO_2 17.49, H_2O 1.04	Amp < 55, Dol 30–35, Mgs 6–14, Cpx 10–30, Grt < 17	CO_2 18.22 wt. %, H_2O < 1.18 wt. %

[a]The observed barian trioctahedral mica (kinoshitalite/Ba-rich phlogopite) is approximated by phlogopite. Its content is not considered in the listed mineral modes. See Kotková et al. (2021a) for the proportions of the minerals in the complete assemblages. The forward thermodynamic models in Fig. 6 are calculated with thermodynamic activity of phlogopite equal to 0.1

[b]The listed contents were used for calculation of the thermodynamic models, with the exception of CO_2 and H_2O. The modelled contents of CO_2 and H_2O are determined by $X(CO_2)$ of a saturated fluid (Fig. 6), or are treated as variables (Fig. 7)

[c]The values correspond to the stability fields of interest in Fig. 6, in which the observed assemblages are stable (labels in bold)

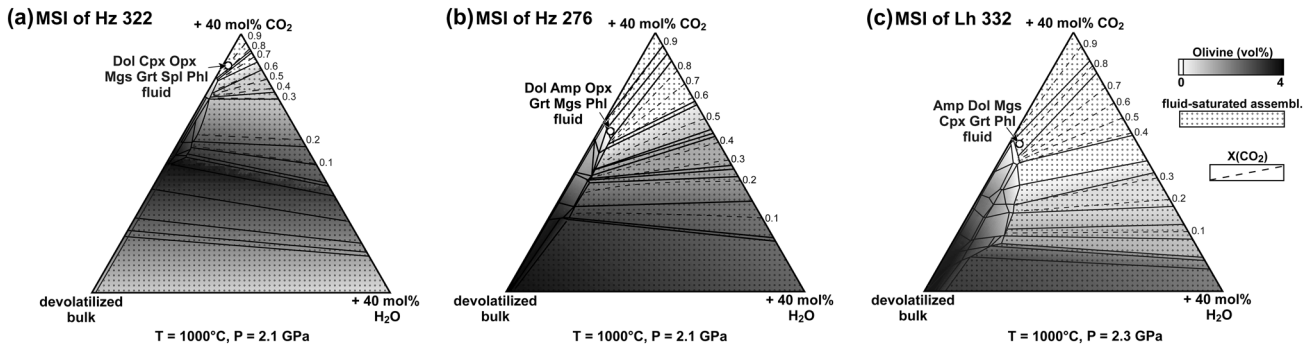

Fig. 7 Forward thermodynamic models calculated at constant P and T designed to investigate the influence of CO_2-H_2O fluid saturation and composition on the stability fields of interest reproduced in Fig. 6 (marked with open circles). Fluid-undersaturated conditions would stabilise olivine, which never occurs in the investigated MSI

The impact of the uncertainties in the bulk composition on the phase equilibria is demonstrated and thoroughly discussed in the Supplementary Document 1 (see Figures S1–S2 and Tables S3–S4). Conclusions from this verification procedure are presented in Fig. 8. Fundamentally, the stability field of the assemblage of interest *Dol Cpx Opx Mgs Grt Chr* is consistently present in all the thermodynamic models calculated for all 10 perturbed compositions (Figure S1). Additionally, each reference stability field overlaps with the original stability field calculated for the unperturbed composition. Also, a small area occurs inside this original stability field, in which all 10 reference models overlap (Fig. 8). The propagation of uncertainty in the bulk composition extended the stability limits of the assemblage of interest to the regions depicted by the dotted area in the Fig. 8a, b. These boundaries were derived from the distribution of the modelled grid points representing the assemblage of interest. They correspond to an area with approximately 95% cumulative probability of the stability of the assemblage of interest (Fig. 8c, d), thus to uncertainty in the bulk composition of 2σ. Regarding the conditions below the solidus curve in Figs. 6a and 8, the upper-pressure stability limit of the assemblage of interest needs to be extended by no more than c. + 0.1 GPa, and the minimum $X(CO_2)$ of the associated fluid decreased by c. 0.1 (Fig. 8b).

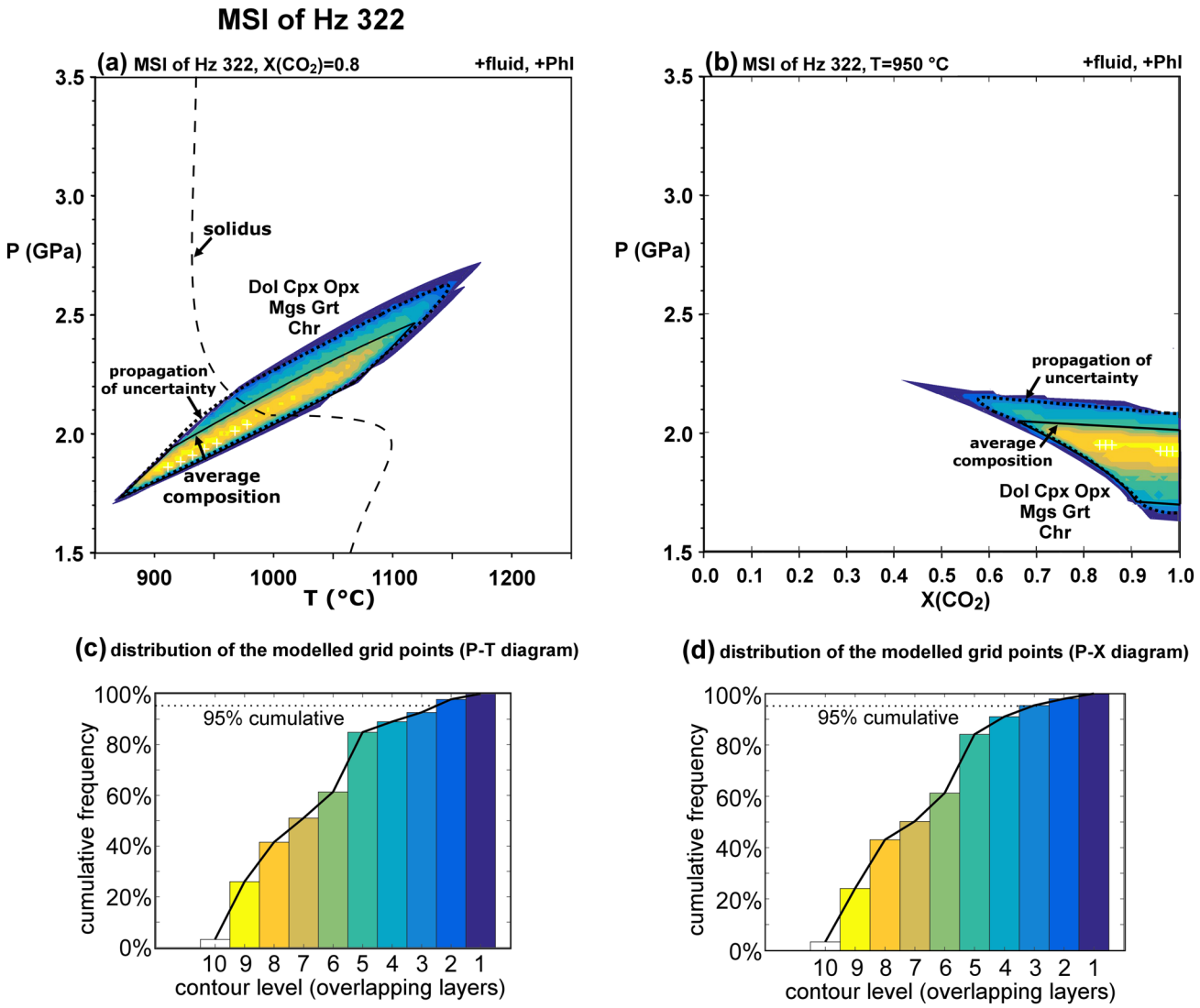

Fig. 8 **a**, **b** Propagation of uncertainties in the mineral proportions in MSI of Hz 322 into the stability limits of the mineral assemblage of interest (*Dol Cpx Opx Mgs Grt Chr*) using a Monte Carlo-type simulation. See text and Supplementary Document 1 for the details of the approach. The solid lines show the stability limits for the average composition, as in Fig. 6a–c, whereas the dashed lines approximate the stability limits corresponding to the uncertainty in mineral proportions of 2σ. These extended stability limits were derived from the distribution of the modelled grid points representing the same stability field of interest in 10 randomised reference models. The dashed lines in **a**, **b** bound areas in which 95% cumulative probability of the stability of the assemblage of interest is reached, as demonstrated in the cumulative frequency bar plots (**c**, **d**). The colour scales (**c**, **d**) depict distinct probability levels—the highest probability of the stability of the mineral assemblage of interest occurs, where all 10 reference models overlap (the brightest zones inside the contour plots in **a**, **b**)

The MSI of Hz 276 are characterised by mineral assemblage *Dol Amp Opx Grt Mgs*. At relatively high $X(CO_2)$ of 0.8–0.9 and sectioning temperature of 950 °C, the upper-pressure boundary of this assemblage is located at c. 2.0–1.8 GPa (Fig. 6d, e). At higher P, orthopyroxene and amphibole disappear, whilst clinopyroxene appears. On the other hand, at lower P, olivine is stable, and dolomite is the only carbonate in the assemblage. Towards the lower $X(CO_2)$ of c. 0.2, the upper pressure boundary shifts to a value of c. 2.6 GPa at 950 °C. However, at even lower $X(CO_2)$ close to 0.1, the stability field becomes shrunk significantly with a P–T maximum of ≤ 900 °C and 2.5 GPa.

Compared to the models for MSI of Hz 322 and MSI of Hz 276, that for MSI of Lh 332 gives less specific information on P–T–$X(CO_2)$ conditions, as the stability fields of all the amphibole-bearing and orthopyroxene-free assemblages present in the latter rock strongly depend on all three system variables. Lherzolite 332 contain MSI comprising *Amp Dol*

Mgs Cpx ± *Grt*, which is projected in the P–T pseudosection calculated for $X(CO_2) = 0.8$ as a relatively narrow field occurring at c. 2.15 GPa at 950 °C (Fig. 6g). At lower pressure, somewhat broader garnet-free field occurs down to c. 1.5 GPa. On the other hand, at higher pressure, amphibole does not participate in the assemblage. Whilst the P–T pseudosections calculated at high $X(CO_2)$ approaching unity provide a minimum pressure estimate, the low $X(CO_2)$ values close to zero yield much higher pressure exceeding 3 GPa (Fig. 6h, i).

The ternary phase diagrams (Fig. 7) with variable proportions of devolatilized rock, H_2O and CO_2, respectively, constructed at fixed T and P (1000 °C, 2.1 GPa for MSI of Hz 322 and 276; 2.3 GPa for MSI of Lh 332), show that the observed mineral assemblages lacking olivine would become unstable in favour of olivine-bearing assemblages if the bulk composition was fluid-undersaturated. Alternatively, at a given P and T, olivine is stabilised at low values of $X(CO_2)$ of the co-existing fluid.

Modelled mineral compositions

The simulated composition parameters of the solid solution phases were extracted from the constructed thermodynamic models, specifically from the stability fields of interest, (Fig. 6a, d, g), and projected as shaded areas in the diagrams in Fig. 5 for comparison with the measured compositions (black markers). The simulated compositions show reasonably good agreement with the observed ones. Both the measured and the simulated garnet compositions fall within the composition range of $Ca_{8\text{-}16}Fe^{2+}{}_{15\text{-}20}Mg_{70\text{-}80}$ (Fig. 5a). Regarding omphacitic clinopyroxene compositions, the models closely reproduce X_{Mg} values as well as Na contents, which are significantly higher in MSI of Lh 332 compared to MSI of Hz 322 (Fig. 5b). Similar to the measured amphiboles, the modelled ones are dominated by the pargasitic component. Reproduction of amphibole composition parameters is very good for MSI of Lh 332 in particular. In case of MSI of Hz 276, the simulated compositions somewhat differ in higher contents of octahedral Al (c.1 apfu) compared to the measured compositions (c. 0.6 apfu). The discrepancy is highly probably influenced by elevated contents of octahedral Cr in the investigated amphibole (c. 0.35 apfu in MSI of Hz 276), which cannot be considered by the model. Additionally, other factors may contribute to propagating the discrepancy, due to the complexity of amphibole mixing behaviour, such as the absence of other elements (e.g. Fe^{3+}) and minor elements in the models and/or the sequential site allocation procedure. The modelled compositions of dolomite and magnesite are very close to the endmembers, like the measured ones (Kotková et al. 2021a). Also, the modelled orthopyroxene is dominated by enstatitic component, as is the measured one. The modelled X_{Mg} in orthopyroxene is lower (c. 0.85–0.87) compared to the measured values (c. 0.94). The discrepancy could be caused by retrogressive modification; the conventional Grt-Opx thermometry also yielded significantly lower temperature compared to the other methods. Also, it may be related to high uncertainty in the value of X_{Mg}, which may be biassed due to incorporation of Fe^{3+}, which is a significant problem for thermobarometry (Canil and O'Neill 1996; Powell and Holland 2008).

Equilibria controlling the field boundaries and mineral compositions, and their dependence on $X(CO_2)$

Obviously, the assemblage from MSI Hz 322 provides the most robust estimate of P and T of equilibration as well as the best constraint on the $X(CO_2)$ of the coexisting fluid. The upper-pressure boundary of this assemblage is controlled by a reaction *enstatite* + *dolomite* = *diopside* + 2 *magnesite* favouring the right-hand side of the equation with increasing pressure. The reaction is responsible for disappearance of orthopyroxene at the boundary (Fig. 6a–c), as it is much less abundant than dolomite. The equilibrium garnet composition is controlled by reaction *pyrope* + 3 *dolomite* = *grossular* + 6 *magnesite*. The two reactions are independent of the $X(CO_2)$ of the fluid, because fluid phase is neither consumed nor produced.

By contrast, the pyroxene-in/out boundary and compositions of amphibole, garnet, pyroxenes and fluid in the pseudosections calculated for the MSI of Hz 276 are related to further, more complex equilibria, such as

2 pargasite + 2 magnesite + 4 CO_2 = 2 pyrope + 3 dolomite + diopside + 2 jadeite + 2 H_2O, or
2 pargasite + 4 magnesite + 4 CO_2 = 2 pyrope + 4 dolomite + enstatite + 2 jadeite + 2 H_2O.

The upper-pressure boundary of the assemblage observed in this harzburgite sample is more sensitive to the composition of the fluid (as the fluid components are involved in the controlling equilibria) and shifts to the maximum pressure at relatively low $X(CO_2)$ of c. 0.3 (Fig. 6e). However, strongly hydrous fluid with $X(CO_2) < 0.2$ cannot co-exist with orthopyroxene at ≥ 900 °C (Fig. 6d–f).

In the case of the orthopyroxene-free MSI assemblages in the studied Lh 332, the upper-pressure boundary is terminal for amphibole, which is the only disappearing phase in the adjacent narrow field, whilst modes of clinopyroxene, garnet and dolomite dramatically increase. The breakdown of this major hydrous phase involves drop of H_2O content

incorporated in the mineral assemblage, whilst phlogopite remains the only hydrous phase above the amphibole-out boundary. However, co-existence of H_2O-dominated fluid would stabilise amphibole to substantially higher pressure compared to the CO_2-dominated fluid (Fig. 6h, i), which makes the mineral assemblage alone a poor indicator of the physico-chemical conditions of the equilibrium.

Impact of the modelled phlogopite activity on the phase equilibria

The reduction of phlogopite activity from 1 to 0.1 has a negligibly small effect on the topology of the pseudosections calculated for MSI of Hz 322 and Lh 332, respectively. The boundaries of the stability fields of interest are displaced by less than ± 0.02 GPa (Figures S3–S4).

A change of the pseudosection topology can be observed in case of MSI of Hz 276. This change includes noticeable shrinkage of the high-temperature part of the stability field of interest (Fig. 6d, see Figure S3b, e for comparison). For the decreased phlogopite activity of 0.1, the higher P–T limit occurs at c. 1025 °C and 2.22 GPa (Fig. 6d), i.e. at lower P–T in comparison to the model calculated with phlogopite activity of 1, where the narrow tip of the stability field reaches c. 1070 °C and 2.7 GPa. On the other hand, the elongated part of this stability field, occurring in the model with phlogopite activity of 1, is assumed to be metastable with respect to a suprasolidus assemblage, as shown in Fig. 6d and discussed below in detail. Moreover, the upper-pressure boundary of the stability field of interest in the relevant temperature range of c. 900–1000 °C shows a relatively minor shift of about − 0.05 GPa with a decrease in phlogopite activity from 1 to 0.1. Thus, the seemingly considerable change in the topology is not interpreted to indicate a significant impact of the phlogopite activity on the stability limits of the mineral assemblage of interest.

As for the modelled compositional parameters, the defined value of phlogopite activity controls potassium content in the system, and consequently in pargasitic amphibole. At a given phlogopite activity, modelled potassium content in amphibole shows increase with increasing temperature. Phlogopite activity equal to unity results in modelled potassium contents exceeding the measured values (0.06 ± 0.02 K apfu) by a factor of 2–5. On the contrary, the measured values are underestimated by a factor of 2–3 with a modelled phlogopite activity of 0.1. Agreement between the measured and modelled values of potassium content in amphibole is achieved for phlogopite activities ranging between 0.2 and 0.3. It is suggested that such deviation from the estimated value around 0.12 is primarily caused by imprecise value of the activity coefficient and/or ordering parameters due to mismatch of the two composition spaces, as mentioned above.

Discussion

Peak conditions experienced by the host rocks, melt entrapment, and P–T path

Our new estimates of the peak P–T conditions experienced by the garnet peridotites sampled by T-7 borehole (c. 4.4–5.7 GPa/1060–1190 °C) somewhat exceed those determined by Medaris et al. (2015). The main cause of this difference is that we utilised the Al-depleted core of scarce Opx_1 porphyroclasts associated with the coupled garnet porphyroclast, whereas Medaris et al. (2015) used matrix orthopyroxene (Opx_2 in this study) with higher Al content. The relatively lower temperatures, obtained through two-pyroxene thermometry, are indicative of exsolution caused by later cooling, which is preserved as lamellae of clinopyroxene in orthopyroxene (Fig. 1c, d).

Our calculations employing MSI-bearing outer parts of garnet and matrix pyroxenes (Opx_2 and Cpx_2) provide pressures of 3.6–4.4 GPa, and pertaining high temperatures of ≥ 1000 °C. These estimates, comparable to the previous peak estimates by Medaris et al. (2015), represent the minimum P–T conditions of the MSI entrapment after up to c. 1 GPa decompression. It is noteworthy, that the pressure estimate of this stage depends on the composition of orthopyroxene and is not much influenced by the change of the composition between the garnet core and the MSI-bearing domain. This relationship is evident from the proximity of the pressure estimates of the peak and the upper-pressure limit for the entrapment, the latter being calculated from MSI-bearing domain in garnet and large pyroxene porphyroclasts (Tables 1, 3).

According to Kotková et al. (2021a), the interaction of the infiltrating liquids with the host rock was essential for the formation of the outer zones of the garnets, and consequently for the entrapment and preservation of the remnants of these evolving liquids as inclusions. We suggest that presence of the liquids could effectively promote re-equilibration and re-crystallisation of the matrix minerals (Ol, Opx_2, Cpx_2), which replaced the rarely preserved peak phases. This idea supports the interpretation that the matrix minerals reflect the conditions of the entrapment of the melts, which took place at the relatively early stage of the exhumation. Simple forward thermodynamic models (pseudosections) of garnet peridotites with a fixed bulk chemical composition lacking CO_2 and H_2O (see e.g. Jennings and Holland 2015) show no production of garnet (i.e. no increase in garnet mode) during decompression from the conditions of c. 1100 °C and > 4 GPa. This argument emphasises the key role of the metasomatic enrichment for the new stage of the garnet growth in the garnet peridotites.

The pressure–temperature conditions obtained from the MSI assemblages, as discussed in the following section, show relatively high temperatures, similar or slightly lower than those at peak or melt entrapment conditions, but they contrast in significantly lower pressures. The contrasting values imply that the exhumation path was characterised by remarkable decompression and much less significant cooling, similar to the UHT-UHP crustal rocks in the area (Haifler and Kotková 2016).

The question of equilibrium amongst the minerals in the MSI and involvement of COH fluid at subsolidus

Above, several equilibria were addressed, which potentially control the stability limits and/or the compositions of the phases occurring in the observed carbonate–silicate mineral assemblages. The forward thermodynamic models imply that these involved endmembers occur as major components participating in equilibrium assemblages, which correspond to the observed assemblages in terms of their mineralogy. If the mineral compositions of the particular assemblage also correspond to equilibrium at specific P–T-X(CO_2), the presented equations must then be applicable for the chemical potentials of the involved endmembers. It could be suggested that mineral proportions in the MSI within a sample vary substantially, leading to high uncertainties in the average compositions. This source of uncertainty has been simulated by the randomly generated reference bulk compositions. In theory, the chemical potentials of the involved endmembers are intensive parameters of the system, meaning they are independent of the amounts of the solution phases in which the endmembers are dissolved. Let's consider an equilibrated assemblage and a theoretical scenario in which the actual mineral proportions appear skewed to the observer due to the sample heterogeneity being beyond the scope of the observation technique. Then, the stability field representing the equilibrium assemblage in a phase diagram constructed for the skewed bulk compositions must overlap with the same field for the actual chemical composition, at least at the specific P–T-X(CO_2). The boundaries of the stability field of interest and the rest of the diagrams may deviate, though. Together, the theoretical example and the Monte Carlo-type simulation imply that the observed carbonate–silicate assemblage may record the physico-chemical conditions of the equilibration regardless of whether the bulk compositions considered for thermodynamic models exactly match the bulk compositions of the original melts. This holds true if the observed mineral assemblages are equilibrium assemblages and if the considered mineral compositions are reasonably close to the equilibrium compositions. In our opinion, both the mineral compositions (Fig. 5) and the mineral modes (Table 4) extracted from the computed thermodynamic models demonstrate reasonably good agreement with the observed and measured mineralogy, considering the necessary simplifications of the composition space and the limited amount of analytical data.

As discussed by Powell and Holland (2008), the forward thermodynamic model employing the internally consistent thermodynamic dataset, is assumed to provide statistically more robust estimates (including evaluation of the uncertainties) compared to the intersection of several conventional thermobarometers. Even though, both methods show reasonably good agreement. Obviously, the amphibole-free MSIs from Hz 322 provide the most straightforward constraints amongst the samples. Both, the forward model and conventional thermobarometry for garnet and clinopyroxene suggest that mineral assemblage and compositions record P–T conditions of c. 900–1100 °C, c. 1.8–2.5 GPa. Moreover, the solids were associated with a COH fluid exhibiting a high $X(CO_2) \geq 0.6$. Additional constraints are imposed based on the position of the experimental solidus (as discussed in the following sections). Thus, the relevant P–T conditions rather correspond to c. 900–1000 °C and c. 1.8–2 GPa, in accordance with the robust forward model.

Comparable P–T-X(CO_2) values reproduce well the amphibole-bearing MSI from Hz 276 and Lh 332, although their stability fields in the models shift to higher pressures (and somewhat lower temperatures) at low X(CO_2) in the fluid. Nevertheless, the composition of COH fluid is not an independent property if the fluid does not behave as a buffer (e.g. Wyllie 1977, 1978). Relatively infrequent occurrence of decrepitation features at the vicinity of the MSI and low porosity within the inclusions (Kotková et al. 2021a; Škoda et al. 2022) imply rather low volumes of involved fluids, i.e. high solid/fluid ratio, which is consistent with low buffering potential of the fluid. On the other hand, participation of a fluid phase and a complete carbonation of the mineral assemblage is documented by the lack of olivine in any MSI from T-7 borehole, as shown by our models (Figs. 6, 7).

Experiments of Tumiati et al. (2013) show similar relationship between the instability of olivine in the carbonated garnet peridotite assemblage and saturation with respect to COH fluid. They suggested that the stable mineral assemblage in their carbonated, hydrated, fluid-saturated, K-enriched peridotite at subsolidus at c. 1000 °C and 2 GPa was *Opx Amp Grt Mag Dol Phl*, in which Dol would disappear and Cpx appear above c. 2.2 GPa (their Fig. 11). This stability field is comparable to our observed assemblage MSI of Hz 276 and our forward model. The equilibrium *enstatite* + *dolomite* = *diopside* + *2 magnesite* controls disappearance of dolomite with increasing pressure for bulk composition investigated by Tumiati et al. (2013), whereas in the

case of bulk compositions of MSI of Hz 322 and MSI of Hz 276 in this study, orthopyroxene is the disappearing phase.

The significance of carbonation reactions for the mineralogy of carbonated peridotites was discussed by Wyllie and Huang (1976) and Wyllie (1977; 1978). These equilibria are responsible for co-existence of peridotitic assemblages with dolomite and magnesite in CO_2-bearing system at pressures above c. 1.8 GPa at 1000 °C. At lower pressure, CO_2 would be accommodated in a vapour phase and the carbonates would not be stable. Obviously, the assemblages in the observed MSI formed at pressures sufficiently high to carbonate the minerals and they did not undergo reverse, decarbonation reactions of this type, which would cause complete degassing of CO_2 (Canil 1990).

As mentioned, the derived P–T stability field of the MSI equilibration constrain the endpoint of the derived decompressional exhumation path. It is noteworthy, that the modelled stability fields are intersected by experimentally determined carbonated (and hydrated) peridotite solidus, as thoroughly discussed in the following section. This coincidence implies that re-equilibration related to terminating crystallisation of the melts established the state of the system. The composition of the trapped melt and its redox conditions, together with the P and T at which solidus was intersected, determined the composition of both, the mineral assemblage, and the exsolved COH fluid. The observed mineralogy of the MSI and the fluid compositions results from the interplay between the carbonated solidus equilibria (Wyllie 1987; Eggler 1978; Olafsson and Eggler 1983; Wallace and Green 1988; Falloon and Green 1990), redox equilibria (Stagno and Frost 2010; Tumiati and Malaspina 2019), carbonation equilibria (Wyllie and Huang 1976; Wyllie 1977) and hydration equilibria (Wyllie 1978).

Calculation of the thermodynamic models at variable phlogopite activities demonstrated a negligible impact on the overall phase equilibria in the case of the amphibole-free assemblage, where the trioctahedral mica is the sole carrier of potassium. Furthermore, the effect is minor in amphibole-bearing assemblages. Potassium strongly prefers incorporation into the trioctahedral mica rather than into amphibole. Thus, the dilute potassium amphibole endmember has a limited influence on the activities of the other endmembers involved in the controlling equilibria, as well as on the stability limits of amphibole in the system. Although the Ba-bearing minerals kinoshitalite/Ba-rich phlogopite (mica), norsethite (carbonate) and celsian (feldspar) are abundant in the MSI (e.g. constituting approximately 51 vol. % in MSI of Hz 322), barium is not significantly involved in other minerals. Therefore, the participation of separate barian phases is not expected to affect the relationships between P, T, and chemical potentials of the major components in dolomite, magnesite, amphibole, garnet and pyroxenes, i.e. the controlling equilibria mentioned above.

Significance of the shape and position of carbonated solidus "ledge"

Published experimental data on (partial) melting of carbonated ultrabasic rocks may approximate the physicochemical conditions and melting behaviour of the systems comparable to the observed MSI at and above the solidus. The experiments show that the solidus curves for these chemical systems are characterised by a so called "carbonate ledge" (Eggler 1987), which is a segment of the curve occurring at a pressure of c. 2–2.5 GPa with a flat, nearly isobaric, or slightly negative dP/dT gradient (Eggler 1978; Wyllie 1987; Wallace and Green 1988; Falloon and Green 1990). The curves are steep and positive at pressures above and below the carbonate ledge. However, the melting temperatures remarkably drop at pressures higher than the ledge (Figs. 6a, d, g, 9), at which CO_2 is soluble in minerals or melt, compared to lower pressures, at which neither mineral assemblages nor melts are carbonated (Wyllie and Huang 1976; Wyllie et al. 1990; Canil 1990). The positions of the carbonate ledge are somewhat variable from one experimental work to another, primarily depending on the considered composition space, the exact bulk composition of the experimental rock, the ratio of CO_2 and H_2O in the fluid and redox conditions (see Hammouda and Keshav 2015 for review). The solidus temperatures for very simple compositions, such as those composed solely of CaO, MgO, SiO_2 and CO_2 (Wyllie and Huang 1976; Eggler 1978), are several hundred Celsius degrees higher compared to temperatures relevant for natural peridotites. The latter (Wallace and Green 1988; Falloon and Green 1990; Pintér et al. 2021) agree well with the positions of stability fields of the MSI mineral assemblages of interest obtained by our forward models. The derived near-isothermal decompressional exhumation path intersects the experimental carbonated solidus curves between c. 950 and 1000 °C at 2–2.2 GPa (Figs. 6a, d, g, 8a, 9).

The evolution of the trapped melts and the crystallisation sequence

For the carbonated and hydrated (ultra)basic systems, such as garnet peridotites and pyroxenites, investigated in this and preceding study by Kotková et al. (2021a), our estimated peak or entrapment P–T conditions, i.e. 4–5.5 GPa and ≥ 1100 °C are sufficient to produce carbonate–silicate melts with compositions comparable to the bulk composition of our observed MSI (Wallace and Green 1988; Foley et al. 2009; Pintér et al. 2021; see Fig. 9). By contrast,

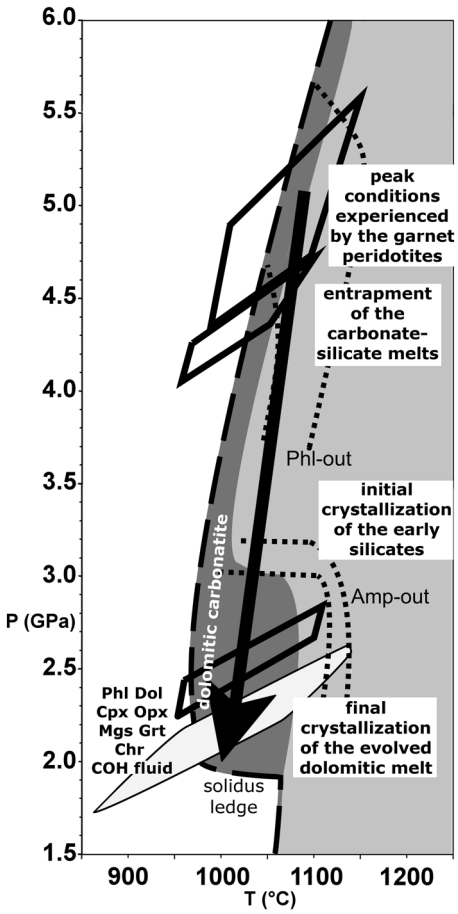

Fig. 9 P–T diagram demonstrating the evolution of the investigated garnet peridotites and the trapped carbonate–silicate melts. The black arrow represents near-isothermal decompressional exhumation path ranging from the peak metamorphic conditions of the rocks, through entrapment of the carbonate–silicate melts, to the melt crystallisation and (re)-equilibration of the MSI assemblages. The stability field of the modelled mineral assemblage reproducing MSI of Hz 322 is shown (see also Fig. 6a–c). The dotted lines depict the upper-P and upper-T experimental stability limits of phlogopite and amphibole in two types of hydrated and carbonated ultramafic rocks: Hawaiian pyrolite (HP) and K-enriched Hawaiian pyrolite (HPK), respectively (Wallace and Green 1988; Pintér et al. 2021). The dark-shaded area represents stability field of a dolomitic carbonatitic melt derived from incipient melting of the carbonated and hydrated peridotite (Pintér et al. 2021). This melt is characterised by relatively low solubility of silicates

volatile-free dry peridotites under the same P–T conditions would remain unmolten (e.g. Hirschmann 2000), as their solidi occur at temperatures by several hundred Celsius degrees higher. Highly probably, the influx of volatile-rich liquids, derived from the subducting slab, served as a trigger of the partial melting of the overlying mantle rocks. As demonstrated by e.g. Green and Wallace (1988) or Gervasoni et al. (2017), infiltration of volatile-(COH)-enriched melts into mantle rocks involves metasomatism and significant chemical changes in both. Subsequently, the pools of melts evolved due to reactive infiltration (Kotková et al. 2021a) were trapped and thus completely isolated by enclosing garnet from the surroundings.

The trapped melt pools in peridotites were highly probably completely molten, lacking refractory unmolten phases, as the MSI do not contain any incidentally trapped phases, neither their minerals occur as monophase inclusions in garnet (e.g. Frezzotti and Ferrando 2015). This is also supported by published experimental data (Wallace and Green 1988; Foley et al. 2009; Pinter et al. 2021): at c. 4 GPa or higher, relatively silica-rich (> 20 wt. % SiO_2, up to c. 40 wt. %) low-degree carbonated melts become stable instead of the initial strictly carbonatitic compositions only c. 90–100 °C above the solidus. As for the solubility of the MSI phases, carbonates are the first to be molten at the experimental solidus. Pargasitic amphibole becomes unstable above c. 3–3.2 GPa both in subsolidus and suprasolidus (Wallace and Green 1988; Niida and Green 1999; Foley et al. 2009; Tumiati et al. 2013; Pintér et al. 2021) although Mandler and Grove (2016) reported its breakdown at higher pressure of c. 3.8 GPa. Phlogopite, a significant component of the observed trioctahedral barian mica, melts at c. 1170 °C/4 GPa (Pintér et al. 2021). It is expected that stability field of kinoshitalite does not exceed these conditions significantly, as Ba shows a strong affinity to the melt (Foley et al. 2009). Omphacitic, jadeite-rich clinopyroxene becomes incompatible with the residuum at c. 1050–1200 °C/3.5–4.5 GPa (Shatskiy et al. 2021; 2022). Indeed, the omphacitic composition of clinopyroxene in the MSI as well as lack of olivine differs from the peridotite residua or subsolidus peridotite, in which olivine is the most abundant phase and clinopyroxene is diopsidic (Pintér et al. 2021). Above, the lack of olivine was attributed to the complete carbonation of the MSI assemblage. However, as forward model (Fig. 7) shows, even in the case the CO_2-rich fluid was absent, the bulk composition of the MSI would provide only minor amounts of olivine (up to c. 4 vol. %). These features agree well with the interpretation that the MSI represent carbonated and hydrated partial melts sequestrated from the residuum.

Although garnet occurs commonly as a residual phase, the experimental carbonate–silicate melts dissolve all garnet constituents including significant amounts of Al_2O_3 (e.g. c. 3–8 wt. % in the K-enriched Hawaiian pyrolite at 1020–1170 °C/4–5 GPa—Foley et al. 2009; Pintér et al. 2021). The observed MSI show somewhat higher Al_2O_3 contents (c. 11–15 wt. %) compared to these reference experimental melts. Another set of experiments on carbonated peridotite by Dasgupta et al. (2007) produced melts with elevated Al_2O_3 contents (c. 9–12 wt. % at ≥ 1325 °C/3 GPa), once the partial melting of garnet took place. It is noteworthy, that the solidus as well as the transition from carbonatitic to carbonate–silicate melts in the anhydrous experimental runs of these authors occurred at significantly

higher temperatures compared to experiments employing CO_2- and H_2O-bearing, and alkali-enriched systems (e.g. Wallace and Green 1988; Foley et al. 2009; Pintér et al. 2021). The obvious differences emphasise the essential role of these components, which participate in the studied MSI, in the onset/degree of melting at particular P and T (e.g. Pintér et al. 2021). The garnet pyroxenite, which served as the initial metasomatic agent in the investigated peridotites, also exhibits relatively high Al_2O_3 content (c. 12 wt. %—Kotková et al. 2021a) and is the probable source of the high aluminosity of the MSI. Consequently, it is suggested that the minor garnet in the MSI precipitated from the trapped melt.

Negative crystal shapes of some MSI imply that an interaction between MSI and host garnet, possibly via a spatially coupled dissolution–re-precipitation reaction mechanism (e.g. Frezzotti 2001; Frezzotti and Ferrando 2015) took place. Our detailed micro-chemical investigation showed no direct evidence of mass transfer between the MSI and the host garnet such as element depletion/enrichment haloes at the adjacent parts of the host. It implies an equilibrium process, as described e.g. by Frezzotti and Ferrando (2015), which did not result in significant modification of the MSI.

The concentric textural relationship exhibited by many inclusions (Fig. 3d, f) implies that the mineral crystallisation was sequential rather than abrupt. As previously discussed by Kotková et al. (2021a), barian mica ± amphibole systematically grow on the walls of the host garnet—either along the walls (Fig. 3d, f, h), or inwards (Fig. 3i), the latter being a feature of crystallisation from a melt (Frezzotti and Ferrando 2015). They likely represent the earliest phases, together with spinel, being followed by further silicates. In Lh 332, later amphibole encloses relatively earlier clinopyroxene (see Fig. 4h in Kotková et al. 2021a). On the contrary, anhedral dolomite and magnesite fill in the spaces between the crystals of the earlier phases (Fig. 3d, f) and highly probably crystallised as the latest major mineral. In addition, the very different element solubilities in carbonated silicate-bearing melts above c. 4 GPa and strictly dolomitic carbonatitic incipient melts at c. 2–2.5 GPa, as obvious from the cited experimental data, clearly show that not only the minerals crystallised sequentially, but the various stages of crystallisation must have occurred at very different pressures. The earlier solid phases highly probably appeared above or close to c. 3 GPa, which is an upper pressure stability limit of pargasitic amphibole (Wallace and Green 1988; Niida and Green 1999; Foley et al. 2009; Tumiati et al. 2013; Pintér et al. 2021; see Fig. 9). At the same time, silicates become much less soluble in the carbonated melts below this pressure (Pintér et al. 2021; Fig. 9). Finally, the late melts approaching the solidus were dominated by dissolved carbonates—especially dolomite, but free of the major silicate components, as observed amounts of silicates in the MSI are insoluble in carbonatitic melts near the solidus. Experimental dolomitic melts co-exist with lherzolitic residua and with phlogopite and amphibole far, up to c. 100 °C above the solidus at 2–2.5 GPa (Wallace and Green 1988; Thibault et al. 1992).

It is noteworthy that the cited experiments were mostly designed to simulate progress of incipient melting of carbonated mantle rocks, usually at an increasing temperature and fixed pressure. Despite differences regarding the compositions of the protoliths, pressure and temperature, or redox conditions, the melts always remain equilibrated with the unmolten residua. In comparison, the solid phases appearing in the MSI after partial crystallisation do not show characteristics of the residua. Although the final carbonatitic melts crystallising in the MSI might have been similar to the incipient experimental melts with regard to their compositions, the process of their formation was different. Evolution of the observed MSI involved magmatic differentiation of isolated, less evolved carbonate–silicate parental melts towards final near-solidus carbonatitic melts. The entire process was controlled by near-isothermal decompression. According to our knowledge, such mechanism of carbonated melt evolution, as well as the effects of the decreased silicate solubility in decompressed carbonated melts, have never been explored experimentally.

Some MSI show polygonal textures, being composed of euhedral mineral grains (Fig. 3b, c; see also Čopjaková and Kotková 2018; Kotková et al. 2021a), which suggests that textural equilibrium was attained amongst the phases, possibly mediated by the late melts close to solidus or by a fluid phase at subsolidus. The reasonable agreement between the forward model and the conventional thermobarometry applied on garnet and clinopyroxene imply that, at least in some cases, also the mineral compositions might have been re-equilibrated or reset since the onset of the sequential crystallisation.

Estimate of redox conditions during the MSI crystallisation

The oxidation state of mantle rocks strongly affects production of melts, potentially serving as a major trigger and controlling factor of melting (e.g. Foley 2011). Oxidising nature of the metasomatizing fluids typical of subduction zone settings (Malaspina et al. 2009; Malaspina and Tumiati 2012; Cannaò and Malaspina 2018; Tumiati and Malaspina 2019) is responsible for mobilisation of carbon as liquid carbonate (e.g. Tumiati and Malaspina 2019; Stagno and Frost 2010) and lowers the melting point significantly compared to the reduced mantle (e.g. Stagno and Frost 2010; Foley 2011; Liu et al. 2023).

According to Stagno and Frost (2010), the equilibrium between solid carbonates, mafic silicates, carbonatitic melt and graphite or diamond at the solidus corresponds roughly to EMOG/D buffer. We assume that their model, giving $\log(fO_2) \approx -10.37$ at 1000 °C, 2.1 GPa for a dolomitic melt, may approximate oxygen fugacity relevant for crystallisation of our MSI. The estimated value is very close to the position of a CCO buffer (Ulmer and Luth 1991), $\log(fO_2) \approx -10.29$ and c. 0.77 log units below FMQ buffer (O'Neill 1987).

Further constraint on redox conditions may be obtained from the estimated composition of the COH fluid associated with the MSI assemblage in the case that it was equilibrated with graphite, as the speciation of the COH fluid is then a function of P, T and oxygen fugacity (e.g. Cesare 1995). Based on the model by Miozzi and Tumiati (2021), the fluid with $X(CO_2) \geq 0.7$ necessary to stabilise assemblage in MSI of Hz 322, corresponds to $\log(fO_2) \geq -11.16$, i.e. ≤ 1.56 log units below FMQ buffer.

Our estimated $f(O_2)$ values represent rather minimum values in case the crystallising melts were more oxidised, and graphite was unstable during the crystallisation (e.g. Malaspina and Tumiati 2012; Tumiati and Malaspina 2019). Although graphite is present in the MSI, its occurrence as films filling intergranular spaces and in decrepitation features (Fig. 4) imply relatively late formation. This may be attributed to the reduction of exsolved and escaping CO_2-rich fluid or the reduction of the carbonate. We suggest that the precipitation of graphite from COH fluid could have taken place due to overstepping the CCO equilibrium (e.g. Malaspina et al. 2009; Malaspina and Tumiati 2012; Tumiati and Malaspina 2019) towards graphite stability field. Such reaction could have occurred during cooling. The results of Raman spectra-based thermometry (Aoya et al. 2010) presented by Škoda et al. (2022) are in a good agreement with this scenario, as they provide relatively low temperatures of graphite formation/recrystallization ≤ 620 °C.

Role of the trapped melts within the carbon cycle

Several recent studies addressed the issue of carbon recycling efficiency via subduction zones (e.g. Dasgupta and Hirschmann 2010; Kelemen and Manning 2015; Plank and Manning 2019; Lara and Dasgupta 2022). These studies agree that significant portions of subducted carbon (probably most according to Kelemen and Manning 2015) are liberated and transported from the subducting slab during its descent to sub-arc depths. Simultaneously, the vast majority (c. 80–95%), of the carbon dissolved in arc magmas and volcanic-arc gases originates from the subduction (Plank and Manning 2019). The overall transportation process between the inputs and outputs may take place within a timeframe of less than 10 Myr (Morris et al. 1990; Marschall and Schumacher 2012; Martin and Hermann 2018). Several authors (e.g. Kelemen and Manning 2015; Scambelluri et al. 2016) have concluded that there is an imbalance between the flux of carbon removed in the subduction zones and flux of carbon returning to the surface via arc magmatism or diffuse outgassing, implying storage of carbon (c. 0–47 Mt/yr according to Kelemen and Manning 2015) in reservoirs occurring in the lithospheric mantle. Therefore, it is worthwhile to evaluate the amount of carbon stored in our investigated rocks.

With regard to the scale of the mantle wedge, the "carbonated solidus ledge" occurs as a relatively narrow zone with a potential to abruptly immobilise molten carbonates. Such melts can infiltrate the overlying mantle during their ascent along the grain boundaries or are transported as trapped melt pools. The investigated MSI record the latter mechanism. They provide evidence of the formation of mobile (liquid) forms of carbon and their subsequent immobilisation via crystallisation of carbonates, accompanied by exsolution of a fraction of subsolidus COH fluid. The host garnet grains effectively shielded the MSI, protecting the carbonate-bearing solid assemblage from further exsolution of CO_2. Due to this effective sequestration mechanism, the duration of the transport of the solidified carbon towards the surface was prolonged. Rock exhumation, erosion, and weathering may significantly delay the liberation of the carbon at the surface by an order of magnitude or more compared to straightforward transport mechanisms of liquid forms of carbon to the surface (e.g. Frezzotti and Touret 2014; Kelemen and Manning 2015; Plank and Manning 2019). The amount of carbon stored in the MSI relative to the host rock can be approximated based on the abundance of the MSI-bearing garnet in the rock, the abundance of the MSI in the garnet, and the average content of the carbonates in the MSI (see Supplementary Document 1 for the details of the calculation). We estimated that lherzolite at the depth of 332 m (Lh 332), representing the predominant lithological type in the peridotite body, contains approximately 0.020 kg C/m^3, (i.e. 0.020 Mt/km^3; 6 ppm) occurring as carbonates in the MSI. Given the widespread and relatively uniform occurrence of the MSI throughout the peridotite drillcore, the estimated values are assumed to be representative of the entire peridotite body, which is about 114 m thick (see the sketch of the borehole in Medaris et al. 2015). The concentration of 6 ppm is about half of the carbon content in the depleted mantle, which was estimated to be around 10–16 ppm (e.g. Salters and Stracke 2004; Workman and Hart 2005; Hirschmann and Dasgupta 2009). If the investigated rocks contained additional carbonates precipitating from the melts during exhumation, without an effective shielding by a host mineral, such unprotected carbonates decomposed at pressure below c. 1.8 GPa, as discussed above.

Apart from their role in flow-driven mass transfer, the carbonated liquids may facilitate rheological weakening and buoyancy of mostly solid-state mantle diapirs and plumes. These bodies were proposed to be another important agent of mass transport, supply of arc-magmas source regions and/or storage of carbon (Gerya and Meilick 2011; Marschall and Schumacher 2012; Tumiati et al. 2013; Codillo et al. 2018; Chen et al. 2021; Ducea et al. 2022).

Conclusions

This paper presents new and refined data for orogenic garnet peridotites encountered in the T-7 borehole in the Saxothuringian Zone of the Bohemian Massif and their interpretation in view of carbonate–silicate melt evolution. The peak metamorphic conditions, P–T conditions of entrapment of multiphase solid inclusions (MSI) in garnet, and P–T conditions of the crystallisation of the MSI assemblages have been estimated at c. 1100 °C/4.5–5.5 GPa, c. 1000 °C/3.6–4.5 GPa, and c. 950–1000 °C/2–2.2 GPa, respectively. These data constrain a near-isothermal decompressional P–T path.

Forward thermodynamic modelling was successfully applied on carbonate–silicate assemblages of the MSI from three peridotite samples. The assemblage *Dol Cpx Opx Mgs Grt Chr* occurring in harzburgite (Hz 322) provided the most robust estimate of the physico-chemical conditions of (re)-equilibration: c. 900–1000 °C/1.8–2.2 GPa and $X(CO_2) \geq 0.6$. Amphibole-bearing assemblages from the two other peridotite samples (Hz 276, Lh 332) were successfully reproduced at the same P–T-$X(CO_2)$ conditions. The modelled P–T stability fields of interest show perfect agreement with the position of a so called "carbonated solidus ledge", which is an isobaric segment of the solidus curve of carbonated peridotite. This coincidence implies that the crystallisation of the melts terminated once the solidus curve was intersected during exhumation along the near-isothermal decompressional P–T path. Comparison with reference melting experiments of carbonated and hydrated peridotites imply, that the crystallisation must have been sequential rather than abrupt due to lower solubility of silicates in the melt at c. 2–3 GPa compared to higher-pressure conditions. Therefore, the initial crystallisation of silicates occurred at higher pressures compared to the crystallisation of the residual dolomitic melt at the solidus ledge. The redox conditions of this final stage of the crystallisation were estimated to be close to CCO buffer or more oxidised.

The investigated carbonate–silicate inclusions provide petrological evidence of a mechanism capable of an abrupt immobilisation of ascending carbonated melts within a relatively narrow zone in the lithospheric mantle. The studied metasomatized peridotites are estimated to store approximately 6 ppm of carbon (i.e. 0.020 kg/m^3 or 0.020 Mt/km^3) occurring as carbonates in the MSI.

Supplementary Information The online version contains supplementary material available at https://doi.org/10.1007/s00410-024-02108-1.

Acknowledgements This research was funded by Czech Science Foundation Project 22-33820S. We acknowledge the constructive comments and suggestions from the journal editor Dante Canil and an anonymous reviewer, which improved the revised version of this article.

Funding Open access publishing supported by the National Technical Library in Prague.

Data availability The authors declare that the data supporting the findings of this study are available within the paper and its attached Supplementary Documents.

References

Ackerman L, Kotková J, Čopjaková R, Sláma J, Trubač J, Dillingerová V (2020) Petrogenesis and Lu-Hf dating of (Ultra)mafic rocks from the Kutná Hora Crystalline Complex: Implications for the devonian evolution of the Bohemian Massif. J Petrol 61:egaa075. https://doi.org/10.1093/petrology/egaa075

Aoya M, Kouketsu Y, Endo S, Shimizu H, Mizukami T, Nakamura D, Wallis S (2010) Extending the applicability of the Raman carbonaceous-material geothermometer using data from contact metamorphic rocks. J Metamorph Geol 28:895–914. https://doi.org/10.1111/j.1525-1314.2010.00896.x

Arculus RJ, Powell R (1986) Source component mixing in the regions of arc magma generation. J Geophys Res Solid Earth 91:5913–5926

Bertrand P, Mercier J-CC (1985) The mutual solubility of coexisting ortho-and clinopyroxene: toward an absolute geothermometer for the natural system? Earth Planet Sci Lett 76:109–122. https://doi.org/10.1016/0012-821X(85)90152-9

Brey GP, Köhler T (1990) Geothermobarometry in four-phase lherzolites II. New thermobarometers, and practical assessment of existing thermobarometers. J Petrol 31:1353–1378. https://doi.org/10.1093/petrology/31.6.1353

Canil D (1990) Experimental study bearing on the absence of carbonate in mantle-derived xenoliths. Geology 18:1011–1013. https://doi.org/10.1130/0091-7613(1990)018%3c1011:ESBOTA%3e2.3.CO;2

Canil D, O'Neill HSC (1996) Distribution of ferric iron in some upper-mantle assemblages. J Petrol 37:609–635. https://doi.org/10.1093/petrology/37.3.609

Cannaò E, Malaspina N (2018) From oceanic to continental subduction: implications for the geochemical and redox evolution of the

supra-subduction mantle. Geosphere 14:2311–2336. https://doi.org/10.1130/GES01597.1
Carswell DA, van Roermund HLM (2005) On multi-phase mineral inclusions associated with microdiamond formation in mantle-derived peridotite lens at Bardane on Fjortoft, west Norway. Eur J Mineral 17:31–42. https://doi.org/10.1127/0935-1221/2005/0017-0031
Cesare B (1995) Graphite precipitation in C–O–H fluid inclusions: closed system compositional and density changes, and thermobarometric implications. Contrib Miner Petrol 122:25–33. https://doi.org/10.1007/s004100050110
Chen C, Förster MW, Foley SF, Liu Y (2021) Massive carbon storage in convergent margins initiated by subduction of limestone. Nat Commun 12:4463. https://doi.org/10.1038/s41467-021-24750-0
Codillo EA, Roux VL, Marschall HR (2018) Arc-like magmas generated by mélange-peridotite interaction in the mantle wedge. Nat Commun 9:2864. https://doi.org/10.1038/s41467-018-05313-2
Connolly JA (2005) Computation of phase equilibria by linear programming: a tool for geodynamic modeling and its application to subduction zone decarbonation. Earth Planet Sci Lett 236:524–541. https://doi.org/10.1016/j.epsl.2005.04.033
Connolly J (2009) The geodynamic equation of state: what and how. Geochem Geophys Geosyst 10:Q10014. https://doi.org/10.1029/2009GC002540
Čopjaková R, Kotková J (2018) Composition of barian mica in multiphase solid inclusions from orogenic garnet peridotites as evidence of mantle metasomatism in a subduction zone setting. Contrib Miner Petrol 173:106. https://doi.org/10.1007/s00410-018-1534-6
Currie CA, Hyndman RD (2006) The thermal structure of subduction zone back arcs. J Geophys Res Solid Earth 111:B08404. https://doi.org/10.1029/2005JB004024
Dasgupta R, Hirschmann MM (2010) The deep carbon cycle and melting in Earth's interior. Earth Planet Sci Lett 298:1–13. https://doi.org/10.1016/j.epsl.2010.06.039
Dasgupta R, Hirschmann MM, Smith ND (2007) Partial melting experiments of peridotite + CO_2 at 3 GPa and genesis of alkalic ocean island basalts. J Petrol 48:2093–2124. https://doi.org/10.1093/petrology/egm053
Ducea MN, Currie CA, Balica C, Lazar I, Mallik A, Petrescu L, Vlasceanu M (2022) Diapirism of carbonate platforms subducted into the upper mantle. Geology 50:929–933. https://doi.org/10.1130/G50000.1
Eggler DH (1978) The effect of CO_2 upon partial melting of peridotite in the system Na_2O-CaO-Al_2O_3-MgO-SiO_2-CO_2 to 35 kb, with an analysis of melting in a peridotite-H_2O-CO_2 system. Am J Sci 278:305–343
Eggler DH (1987) Discussion of recent papers on carbonated peridotite, bearing on mantle metasomatism and magmatism: an alternative. Earth Planet Sci Lett 82:398–400. https://doi.org/10.1016/0012-821X(87)90214-7
Falloon TJ, Green DH (1990) Solidus of carbonated fertile peridotite under fluid-saturated conditions. Geology 18:195–199. https://doi.org/10.1130/0091-7613(1990)018%3c0195:SOCFPU%3e2.3.CO;2
Foley SF (2011) A reappraisal of redox melting in the earth's mantle as a function of tectonic setting and time. J Petrol 52:1363–1391. https://doi.org/10.1093/petrology/egq061
Foley SF, Yaxley GM, Rosenthal A, Buhre S, Kiseeva ES, Rapp RP, Jacob DE (2009) The composition of near-solidus melts of peridotite in the presence of CO_2 and H_2O between 40 and 60 kbar. Lithos 112:274–283. https://doi.org/10.1016/j.lithos.2009.03.020
Franzolin E, Schmidt M, Poli S (2011) Ternary Ca–Fe–Mg carbonates: subsolidus phase relations at 3.5 GPa and a thermodynamic solid solution model including order/disorder. Contrib Miner Petrol 161:213–227. https://doi.org/10.1007/s00410-010-0527-x
Frezzotti M-L (2001) Silicate-melt inclusions in magmatic rocks: applications to petrology. Lithos 55:273–299. https://doi.org/10.1016/S0024-4937(00)00048-7
Frezzotti ML, Ferrando S (2015) The chemical behavior of fluids released during deep subduction based on fluid inclusions. Am Miner 100:352–377. https://doi.org/10.2138/am-2015-4933
Frezzotti ML, Touret JLR (2014) CO_2, carbonate-rich melts, and brines in the mantle. Geosci Front 5:697–710. https://doi.org/10.1016/j.gsf.2014.03.014
Fumagalli P, Zanchetta S, Poli S (2009) Alkali in phlogopite and amphibole and their effects on phase relations in metasomatized peridotites: a high-pressure study. Contrib Miner Petrol 158:723–737. https://doi.org/10.1007/s00410-009-0407-4
Gervasoni F, Klemme S, Rohrbach A, Grützner T, Berndt J (2017) Experimental constraints on mantle metasomatism caused by silicate and carbonate melts. Lithos 282–283:173–186. https://doi.org/10.1016/j.lithos.2017.03.004
Gerya TV, Meilick FI (2011) Geodynamic regimes of subduction under an active margin: effects of rheological weakening by fluids and melts. J Metamorph Geol 29:7–31. https://doi.org/10.1111/j.1525-1314.2010.00904.x
Gibson SA, McKenzie D (2023) On the role of Earth's lithospheric mantle in global volatile cycles. Earth Planet Sci Lett 602:117946. https://doi.org/10.1016/j.epsl.2022.117946
Gorman PJ, Kerrick D, Connolly J (2006) Modeling open system metamorphic decarbonation of subducting slabs. Geochem Geophys Geosyst 7:Q04007. https://doi.org/10.1029/2005GC001125
Green DH, Wallace ME (1988) Mantle metasomatism by ephemeral carbonatite melts. Nature 336:459–462. https://doi.org/10.1038/336459a0
Green E, White R, Diener J, Powell R, Holland T, Palin R (2016) Activity–composition relations for the calculation of partial melting equilibria in metabasic rocks. J Metamorph Geol 34:845–869. https://doi.org/10.1111/jmg.12211
Haifler J, Kotková J (2016) UHP-UHT peak conditions and near-adiabatic exhumation path of diamond-bearing garnet-clinopyroxene rocks from the Eger Crystalline Complex, North Bohemian Massif. Lithos 248–251:366–381. https://doi.org/10.1016/j.lithos.2016.02.001
Hammouda T, Keshav S (2015) Melting in the mantle in the presence of carbon: review of experiments and discussion on the origin of carbonatites. Chem Geol 418:171–188. https://doi.org/10.1016/j.chemgeo.2015.05.018
Hammouda T, Manthilake G, Goncalves P, Chantel J, Guignard J, Crichton W, Gaillard F (2021) Is there a global carbonate layer in the oceanic mantle? Geophys Res Lett 48:e2020GL089752. https://doi.org/10.1029/2020GL089752
Harley SL (1984) An experimental study of the partitioning of Fe and Mg between garnet and orthopyroxene. Contrib Miner Petrol 86:359–373. https://doi.org/10.1007/BF01187140
Hirschmann MM (2000) Mantle solidus: experimental constraints and the effects of peridotite composition. Geochem Geophys Geosyst 1:2000GC000070. https://doi.org/10.1029/2000GC000070
Hirschmann MM, Dasgupta R (2009) The H/C ratios of Earth's near-surface and deep reservoirs, and consequences for deep Earth volatile cycles. Chem Geol 262:4–16. https://doi.org/10.1016/j.chemgeo.2009.02.008
Holland T, Powell R (1991) A Compensated-Redlich-Kwong (CORK) equation for volumes and fugacities of CO_2 and H_2O in the range 1 bar to 50 kbar and 100–1600°C. Contrib Miner Petrol 109:265–273. https://doi.org/10.1007/BF00306484
Holland T, Powell R (2011) An improved and extended internally consistent thermodynamic dataset for phases of petrological interest, involving a new equation of state for solids. J Metamorph Geol 29:333–383. https://doi.org/10.1111/j.1525-1314.2010.00923.x

Holland TJ, Green EC, Powell R (2018) Melting of peridotites through to granites: a simple thermodynamic model in the system KNCFMASHTOCr. J Petrol 59:881–900. https://doi.org/10.1093/petrology/egy048

Jennings ES, Holland TJ (2015) A simple thermodynamic model for melting of peridotite in the system NCFMASOCr. J Petrol 56:869–892. https://doi.org/10.1093/petrology/egv020

Johnston FKB, Turchyn AV, Edmonds M (2011) Decarbonation efficiency in subduction zones: implications for warm Cretaceous climates. Earth Planet Sci Lett 303:143–152. https://doi.org/10.1016/j.epsl.2010.12.049

Kelemen PB, Manning CE (2015) Reevaluating carbon fluxes in subduction zones, what goes down, mostly comes up. Proc Natl Acad Sci USA 112:E3997–E4006. https://doi.org/10.1073/pnas.1507889112

Kerrick D, Connolly J (2001) Metamorphic devolatilization of subducted marine sediments and the transport of volatiles into the Earth's mantle. Nature 411:293–296. https://doi.org/10.1038/35077056

Kotková J, O'Brien PJ, Ziemann MA (2011) Diamond and coesite discovered in Saxony-type granulite: solution to the Variscan garnet peridotite enigma. Geology 39:667–670. https://doi.org/10.1130/G31971.1

Kotková J, Čopjaková R, Škoda R (2021a) Multiphase solid inclusions reveal the origin and fate of carbonate-silicate melts in metasomatised peridotite. Lithos 398–399:106309. https://doi.org/10.1016/j.lithos.2021.106309

Kotková J, Fedortchouk Y, Wirth R, Whitehouse MJ (2021b) Metamorphic microdiamond formation is controlled by water activity, phase transitions and temperature. Sci Rep 11:7694. https://doi.org/10.1038/s41598-021-87272-1

Lara M, Dasgupta R (2022) Carbon recycling efficiency in subduction zones constrained by the effects of H2O-CO2 fluids on partial melt compositions in the mantle wedge. Earth Planet Sci Lett 588:117578. https://doi.org/10.1016/j.epsl.2022.117578

Liu Z, Rohrbach A, Tiraboschi C, Foley SF, Berndt J, Klemme S (2023) The effect of COH fluids on partial melting of eclogite and lherzolite under moderately oxidizing and reducing conditions. Chem Geol 616:121219. https://doi.org/10.1016/j.chemgeo.2022.121219

Malaspina N, Tumiati S (2012) The role of C-O-H and oxygen fugacity in subduction-zone garnet peridotites. Eur J Mineral 24:607–618. https://doi.org/10.1127/0935-1221/2012/0024-2213

Malaspina N, Hermann J, Scambelluri M, Compagnoni R (2006) Polyphase inclusions in garnet-orthopyroxenite (Dabie Shan, China) as monitors for metasomatism and fluid-related trace element transfer in subduction zone peridotite. Earth Planet Sci Lett 249:173–187. https://doi.org/10.1016/j.epsl.2006.07.017

Malaspina N, Poli S, Fumagalli P (2009) The oxidation state of metasomatized mantle wedge: Insights from C-O-H-bearing garnet peridotite. J Petrol 50:1533–1552. https://doi.org/10.1093/petrology/egp040

Mandler BE, Grove TL (2016) Controls on the stability and composition of amphibole in the Earth's mantle. Contrib Miner Petrol 171:68. https://doi.org/10.1007/s00410-016-1281-5

Marschall HR, Schumacher JC (2012) Arc magmas sourced from mélange diapirs in subduction zones. Nat Geosci 5:862–867. https://doi.org/10.1038/ngeo1634

Martin LAJ, Hermann J (2018) Experimental phase relations in altered oceanic crust: Implications for carbon recycling at subduction zones. J Petrol 59:299–320. https://doi.org/10.1093/petrology/egy031

Medaris LG, Ackerman L, Jelínek E, Michels ZD, Erban V, Kotková J (2015) Depletion, cryptic metasomatism, and modal metasomatism (refertilization) of Variscan lithospheric mantle: Evidence from major elements, trace elements, and Sr-Nd-Os isotopes in a Saxothuringian garnet peridotite. Lithos 226:81–97. https://doi.org/10.1016/j.lithos.2014.10.007

Merlet C (1994) An accurate computer correction program for quantitative electron probe analysis. Microchim Acta 114:363–376. https://doi.org/10.1007/BF01244563

Miozzi F, Tumiati S (2021) Aqueous concentration of CO_2 in carbon-saturated fluids as a highly sensitive oxybarometer. Geochem Perspect Lett 16:30–34. https://doi.org/10.7185/GEOCHEMLET.2040

Modreski PJ, Boettcher A (1973) Phase relationships of phlogopite in the system K_2O-MgO-CaO-Al_2O_3-SiO_2-H_2O to 35 kilobars; a better model for micas in the interior of the Earth. Am J Sci 273:385–414. https://doi.org/10.2475/ajs.273.5.385

Morris JD, Leeman WP, Tera F (1990) The subducted component in island arc lavas: constraints from Be isotopes and B-Be systematics. Nature 344:31–36. https://doi.org/10.1038/344031a0

Naemura K, Hirajima T, Svojtka M, Shimizu I, Iizuka T (2018) Fossilized melts in mantle wedge peridotites. Sci Rep 8:10116. https://doi.org/10.1038/s41598-018-28264-6

Nickel KG, Green DH (1985) Empirical geothermobarometry for garnet peridotites and implications for the nature of the lithosphere, kimberlites and diamonds. Earth Planet Sci Lett 73:158–170. https://doi.org/10.1016/0012-821X(85)90043-3

Niida K, Green DH (1999) Stability and chemical composition of pargasitic amphibole in MORB pyrolite under upper mantle conditions. Contrib Miner Petrol 135:18–40. https://doi.org/10.1007/s004100050495

Nimis P, Taylor WR (2000) Single clinopyroxene thermobarometry for garnet peridotites. Part I. Calibration and testing of a Cr-in-Cpx barometer and an enstatite-in-Cpx thermometer. Contrib Miner Petrol 139:541–554. https://doi.org/10.1007/s004100000156

O'Neill HSC (1987) Quartz-fayalite-iron and quartz-fayalite-magnetite equilibria and the free energy of formation of fayalite (Fe_2SiO_4) and magnetite (Fe_3O_4). Am Miner 72:67–75

O'Neill HSC, Wood B (1979) An experimental study of Fe-Mg partitioning between garnet and olivine and its calibration as a geothermometer. Contrib Miner Petrol 70:59–70. https://doi.org/10.1007/BF00371872

Olafsson M, Eggler DH (1983) Phase relations of amphibole, amphibole-carbonate, and phlogopite-carbonate peridotite: petrologic constraints on the asthenosphere. Earth Planet Sci Lett 64:305–315. https://doi.org/10.1016/0012-821X(83)90212-1

Palin RM, Weller OM, Waters DJ, Dyck B (2016) Quantifying geological uncertainty in metamorphic phase equilibria modelling; a Monte Carlo assessment and implications for tectonic interpretations. Geosci Front 7:591–607. https://doi.org/10.1016/j.gsf.2015.08.005

Pintér Z, Foley SF, Yaxley GM, Rosenthal A, Rapp RP, Lanati AW, Rushmer T (2021) Experimental investigation of the composition of incipient melts in upper mantle peridotites in the presence of CO_2 and H_2O. Lithos 396–397:106224. https://doi.org/10.1016/j.lithos.2021.106224

Plank T, Manning CE (2019) Subducting carbon. Nature 574:343–352. https://doi.org/10.1038/s41586-019-1643-z

Powell R (1985) Regression diagnostics and robust regression in geothermometer/geobarometer calibration: the garnet-clinopyroxene geothermometer revisited. J Metamorph Geol 3:231–243. https://doi.org/10.1111/j.1525-1314.1985.tb00319.x

Powell R, Holland T (1999) Relating formulations of the thermodynamics of the mineral solid solutions; activity modeling of pyroxenes, amphiboles, and micas. Am Miner 84:1–14. https://doi.org/10.2138/am-1999-1-201

Powell R, Holland T (2008) On thermobarometry. J Metamorph Geol 26:155–179. https://doi.org/10.1111/j.1525-1314.2007.00756.x

Salters VJM, Stracke A (2004) Composition of the depleted mantle. Geochem Geophys Geosyst 5:Q0507. https://doi.org/10.1029/2003GC000597

Scambelluri M, Bebout GE, Belmonte D, Gilio M, Campomenosi N, Collins N, Crispini L (2016) Carbonation of subduction-zone serpentinite (high-pressure ophicarbonate; Ligurian Western Alps) and implications for the deep carbon cycling. Earth Planet Sci Lett 441:155–166. https://doi.org/10.1016/j.epsl.2016.02.034

Shatskiy A, Podborodnikov IV, Arefiev AV, Bekhtenova A, Vinogradova YG, Stepanov KM, Litasov KD (2021) Pyroxene-carbonate reactions in the $CaMgSi_2O_6 \pm NaAlSi_2O_6 + MgCO_3 \pm Na_2CO_3 \pm K_2CO_3$ system at 3–6 GPa: implications for partial melting of carbonated peridotite. Contrib Miner Petrol 176:34. https://doi.org/10.1007/s00410-021-01790-9

Shatskiy A, Bekhtenova A, Arefiev AV, Podborodnikov IV, Vinogradova YG, Rezvukhin DI, Litasov KD (2022) Solidus and melting of carbonated phlogopite peridotite at 3–6.5 GPa: Implications for mantle metasomatism. Gondwana Res 101:156–174. https://doi.org/10.1016/j.gr.2021.07.023

Škoda R, Čopjaková R, Kotková J, Wirth R (2022) Graphite formation from CO_2-rich fluid in metasomatized mantle. In: Angiboust S (ed.) 14th International Eclogite Conference. Book of Abstracts. Lyon, France, 10–13 July 2022

Spandler C, Pirard C (2013) Element recycling from subducting slabs to arc crust: a review. Lithos 170–171:208–223. https://doi.org/10.1016/j.lithos.2013.02.016

Stagno V, Frost DJ (2010) Carbon speciation in the asthenosphere: experimental measurements of the redox conditions at which carbonate-bearing melts coexist with graphite or diamond in peridotite assemblages. Earth Planet Sci Lett 300:72–84. https://doi.org/10.1016/j.epsl.2010.09.038

Syracuse EM, van Keken PE, Abers GA (2010) The global range of subduction zone thermal models. Phys Earth Planet Inter 183:73–90. https://doi.org/10.1016/j.pepi.2010.02.004

Thibault Y, Edgar AD, Lloyd FE (1992) Experimental investigation of melts from a carbonated phlogopite lherzolite: implications for metasomatism in the continental lithospheric mantle. Am Miner 77:784–794

Tumiati S, Malaspina N (2019) Redox processes and the role of carbon-bearing volatiles from the slab–mantle interface to the mantle wedge. J Geol Soc 176:388–397. https://doi.org/10.1144/jgs2018-046

Tumiati S, Fumagalli P, Tiraboschi C, Poli S (2013) An experimental study on COH-bearing peridotite up to 3.2 GPa and implications for crust-mantle recycling. J Petrol 54:453–479. https://doi.org/10.1093/petrology/egs074

Ulmer P, Luth RW (1991) The graphite-COH fluid equilibrium in P, T, space: an experimental determination to 30 kbar and 1600 °C. Contrib Miner Petrol 106:265–272. https://doi.org/10.1007/BF00324556

Wallace PJ (2005) Volatiles in subduction zone magmas: concentrations and fluxes based on melt inclusion and volcanic gas data. J Volcanol Geoth Res 140:217–240. https://doi.org/10.1016/j.jvolgeores.2004.07.023

Wallace ME, Green DH (1988) An experimental determination of primary carbonatite magma composition. Nature 335:343–346. https://doi.org/10.1038/335343a0

Warr LN (2021) IMA–CNMNC approved mineral symbols. Mineral Mag 85:291–320. https://doi.org/10.1180/mgm.2021.43

Workman RK, Hart SR (2005) Major and trace element composition of the depleted MORB mantle (DMM). Earth Planet Sci Lett 231:53–72. https://doi.org/10.1016/j.epsl.2004.12.005

Wu C, Zhao G (2007) A recalibration of the garnet-olivine geothermometer and a new geobarometer for garnet peridotites and garnet-olivine-plagioclase-bearing granulites. J Metamorph Geol 25:497–505. https://doi.org/10.1111/j.1525-1314.2007.00706.x

Wyllie PJ (1977) Mantle fluid compositions buffered by carbonates in peridotite-CO_2-H_2O. J Geol 85:187–207

Wyllie PJ (1978) Mantle fluid compositions buffered in peridotite-CO_2-H_2O by carbonates, amphibole, and phlogopite. J Geol 86:687–713

Wyllie PJ (1987) Discussion of recent papers on carbonated peridotite, bearing on mantle metasomatism and magmatism. Earth Planet Sci Lett 82:391–397. https://doi.org/10.1016/0012-821X(87)90213-5

Wyllie PJ, Huang W-L (1976) Carbonation and melting reactions in the system CaO-MgO-SiO_2-CO_2 at mantle pressures with geophysical and petrological applications. Contrib Miner Petrol 54:79–107. https://doi.org/10.1007/BF00372117

Wyllie PJ, Baker MB, White BS (1990) Experimental boundaries for the origin and evolution of carbonatites. Lithos 26:3–19. https://doi.org/10.1016/0024-4937(90)90037-2